

ABSTRACT

VAISH, MAYANK. Lung-Aerosol Dynamics in Human Airway Models: Validation and Application of OpenFOAM Software. (Under the direction of Dr. Clement Kleinstreuer).

The goal of this study is to explore and validate OpenFOAM software, using the lung-aerosol dynamics project of the Computational Multi-Physics Lab (MAE Department, NC State University, Raleigh, NC) as an application. OpenFOAM is an open-source CFD toolbox written in C++, taking advantage of the object-oriented nature of this programming language. A series of validations have been done to build confidence in this software before developing and presenting new results. The human respiratory tract is a geometrically complex assemblage of airways, including nasal and oral airways, the trachea, and 23 generations. Various physical models exist, starting with symmetric models where the mesh generation process is easy and computations are quick; but, results are not realistic and accurate. Thus, subject-specific geometries are preferred; however, the mesh generation process is tedious and the computer simulation times are taxing. In the first research phase, OpenFOAM steady-state solver (*simpleFoam*), transient solver (*pimpleFoam*), Lagrangian particle tracking solver (*icoUncoupledKinematicParcelFoam*) and transitional turbulence model (*kkLOmega*) were validated against published experimental data sets to test the suitability of OpenFOAM solvers with regard to previous lung-aerosol dynamics results. Specifically, simulations were performed using the Weibel Type A model, a patient-specific geometry (Cheng et al., 1999) and a trumpet model representing the entire respiratory system. A novel contribution was made in case of the trumpet model, where a mathematical correlation for the radial force, in terms of particle diameter, lung volume and breathing pattern, was developed. It was then applied to the trumpet model geometry, yielding deposition data that agree well with *in vivo* experimental

results. Clearly, this 1-D approach saves time and computational resources. Also, comparisons are presented between simulation results with OpenFOAM and the commercial solver CFX (Ansys, Inc. Canonsburg, PA) for one steady and one transient case, focusing on clock time and accuracy.

© Copyright 2014 by Mayank Vaish

All Rights Reserved

Lung-Aerosol Dynamics in Human Airway Models: Validation and Application of
OpenFOAM Software

by
Mayank Vaish

A thesis submitted to the Graduate Faculty of
North Carolina State University
in partial fulfillment of the
requirements for the degree of
Master of Science

Mechanical Engineering

Raleigh, North Carolina

2014

APPROVED BY:

Dr. Clement Kleinstreuer
Committee Chair

Dr. Brendan T. O'Connor

Dr. Yun Jing

DEDICATION

*I dedicate this thesis to my parents and sister for their
unconditional love and support.*

BIOGRAPHY

The author, son of Om Prakash and Rekha Vaish and younger brother to Tanushree Gupta, was born on 16th November 1988 in the city of Lucknow, capital of the state of Uttar Pradesh, India. He attended high school at City Montessori School, Lucknow and Modi Public School, Kota. To pursue undergraduate study in Mechanical Engineering he moved to New Delhi and went to Delhi College of Engineering. After the college completed he worked in India's leading automotive company, Maruti Suzuki India Ltd. as Graduate Engineer Trainee in HVAC Design Group. He went back to school at North Carolina State University to pursue MS degree in Mechanical Engineering. After pursuing a year of coursework he started doing research under the direction of Dr. Clement Kleinstreuer. After the completion of his degree program he will pursue a career in industrial research related to Fluid Dynamics.

ACKNOWLEDGMENTS

First and foremost, I would like to express my deep gratitude to my advisor, Dr. Clement Kleinstreuer, for his encouragement, guidance, and support throughout my graduate study. This work has been possible only due to the enormous support and patience provided by him. I would also like to express my gratitude to Dr. Brendan T. O'Connor and Dr. Yun Jing for taking time from their schedule to be a part of my thesis committee.

I would also like to thank the people who have helped me in various ways during my work on this Master's Thesis. First of all I would like to thank Dr. Emily Childress, Dr. Yu Feng, Arun Varghese Kolanjiyil, Luke Xu, Tejas Umbarkar, Xiaole Chen, Nadish Saini and Narsimha Rao P V P for all the help, support and explanations. I am very thankful to my friends who have been very supportive and accommodating.

I would like to thank my family for all their support throughout my education, with special thanks to my beloved parents and sister for their love, advice and financial support.

TABLE OF CONTENTS

LIST OF TABLES	viii
LIST OF FIGURES	ix
ABBREVIATIONS AND SYMBOLS.....	xii

CHAPTER 1

INTRODUCTION AND OVERVIEW

1.1 Research Motivation	1
1.2 Research Objectives.....	1
1.3 Basic Human Lung Morphology	2
1.4 Literature Review.....	3
1.4.1 Geometrical Lung Models	3
1.4.2 Airflow Structures.....	5
1.4.3 Particle Deposition.....	8

CHAPTER 2

FLUID FLOW AND PARTICLE TRANSPORT

2.1 Fluid Flow Equations.....	12
2.2 Particle Transport.....	13
2.3 Particle Interactions	16
2.4 Particle Forces.....	17
2.5 Particle Deposition Mechanisms.....	21

CHAPTER 3

COMPUTER MODEL VALIDATIONS

3.1 OpenFOAM	24
3.1.1 Introduction and Overview.....	25
3.1.2 Mesh Generation	25
3.1.3 OpenFOAM Solvers.....	27
3.1.4 Post-Processing	29
3.1.5 Modular OpenFOAM Case Structure.....	30
3.2 Case A: Steady-State Airflow Fields	33
3.2.1 Geometry and Mesh.....	33
3.2.2 Governing Equations, Boundary Conditions and Numerical Schemes ..	34
3.2.3 Results and Discussion	35
3.3 Case B: Transient Airflow Fields	39

3.3.1	Governing Equations, Boundary Conditions and Numerical Schemes .	39
3.3.2	Results and Discussion	40
3.4	Case C: Airflow Field with Particle Distribution	45
3.4.1	Geometry and Mesh.....	45
3.4.2	Governing Equations, Boundary Conditions and Numerical Schemes .	46
3.4.3	Results and Discussion	47
3.5	Case D: Particle Deposition in Double and Triple Bifurcations.....	48
3.5.1	Geometry and Mesh.....	48
3.5.2	Governing Equation, Boundary Condition and Numerical Scheme	49
3.5.3	Results and Discussion.....	49
3.6	Software Performance Analysis: CFX vs. OpenFOAM	53
3.6.1	Results: Coarse Mesh	54
3.6.2	Results: Fine Mesh	55

CHAPTER 4

OpenFOAM SOFTWARE APPLICATIONS

4.1	Turbulence Model Validation	58
4.1.1	Geometry and Mesh.....	58
4.1.2	Governing Equation, Boundary Condition and Numerical Scheme	59
4.1.3	Results and Discussion	61
4.2	Trumpet Model	66
4.2.1	Novel Approach and Methodology.....	68
4.2.2	Geometry and Mesh.....	68
4.2.3	Governing Equation, Boundary Condition and Numerical Scheme.....	69
4.2.4	Results and Discussions.....	69

CHAPTER 5

COMPARISON OF PARTICLE DEPOSITION SIMULATION RESULTS WITH *IN VIVO* EXPERIMENTAL STUDIES

5.1	Microsphere Deposition in Patient Specific Airway Geometry	76
5.1.1	Geometry and Mesh.....	76
5.1.2	Governing Equation, Boundary Condition and Numerical Scheme.....	77
5.1.3	Results and Discussions.....	80
5.2	Conclusions and Future Works.....	83
5.2.1	Conclusions.....	83
5.2.2	Future Works	85

REFERENCES	87
APPENDIX A.....	91
A.1 <i>kkLOmega</i> Turbulence Model Equations.....	91

LIST OF TABLES

TABLE 3.1: List of OpenFOAM mesh converter commands	25
TABLE A.1: <i>kkLOmega</i> Turbulence Model Constants	96

LIST OF FIGURES

Fig 1.4(a): Velocity Distribution Contours in an Oral Airway Model.....	11
Fig 3.1(a): OpenFOAM Case Structure	30
Fig 3.2(a): Case A Geometry	34
Fig 3.2(b): Case A Velocity Profile at A-A'	36
Fig 3.2 (c): Case A Velocity Profile at B-B'	36
Fig 3.2 (d): Case A Velocity Vector Representation	37
Fig 3.2 (e): Case A Probe Location at C-C'	37
Fig 3.2 (f): Case A Transverse Plane Velocity Profile at C-C'	38
Fig 3.3(a). Case B Input Waveform	40
Fig 3.3(b): Case B Probe Locations	41
Fig 3.3(c): Case B Velocity Profile at Station 2, 0.2T (3.9s)	41
Fig 3.3(d): Case B Velocity Profile at Station 10, 0.2T (3.9s).....	42
Fig 3.3(e): Case B Velocity Profile at Station 15, 0.2T (3.9s)	43
Fig 3.3(f): Case B Velocity Profile at Station 2, 0.7T (13.7s).....	44
Fig 3.3(g): Case B Velocity Profile at Station 10, 0.7T (13.7s).....	44
Fig 3.4(a): Case C Geometry Schematic	46
Fig 3.4(b): Case C Result	47
Fig 3.5: Case D Representative Geometries.....	48
Fig 3.5(a): Double bifurcation (Kim and Fisher, 1999)	48
Fig 3.5(b): Triple Bifurcation (Zhang et al,2001)	48

Fig 3.5 (c): Case D Particle Deposition in First Bifurcation	50
Fig 3.5 (d): Case D Particle Deposition in Second Bifurcation	51
Fig 3.5 (e): Case D Particle Deposition in First Bifurcation	51
Fig 3.5 (f): Case D Particle Deposition in Second Bifurcation	52
Fig 3.5 (g): Case D Particle Deposition in Third Bifurcation	52
Fig 3.5 (h): Case D Particle Deposition Pattern in Third Bifurcation.....	53
Fig 3.6 (a): Coarse Mesh Comparison at A-A'	54
Fig 3.6 (b): Coarse Mesh Comparison at B-B'	55
Fig 3.6 (c): Fine Mesh Comparison at A-A'	55
Fig 3.6 (d): Fine Mesh Comparison at B-B'	56
Fig 4.1(a): Turbulence Model Validation Geometry Schematic.....	59
Fig 4.1(b): Turbulence Model Validation Result Probe locations	61
Fig 4.1(c): Turbulence Model Validation Result at z=0, Re=500.....	61
Fig 4.1(d): Turbulence Model Validation Result at z=D, Re=500	62
Fig 4.1(e): Turbulence Model Validation Result at z=4D, Re=500.....	62
Fig 4.1(f): Turbulence Model Validation Result at z=0, Re=2000	63
Fig 4.1(g): Turbulence Model Validation Result at z=D, Re=2000.....	64
Fig 4.1(h): Turbulence Model Validation Result at z=2.5D, Re=2000	64
Fig 4.1(i): Turbulence Model Validation Result at z=6D, Re=2000.....	65
Fig 4.2(a): One dimensional trumpet model (Hofmann, 2011).....	67
Fig 4.2(b): Particle Deposition Fraction at 30L/min, 15 L/min	71

Fig 4.2(c): Particle Deposition Fraction at 15 L/min and tidal volume of 500ml, 1000ml...	72
Fig 4.2(d): Particle Deposition Fraction at 15 L/min and total lung volume of 4000ml, 3000ml	74
Fig 5.1(a): Model II Geometry (Feng and Kleinstreuer, 2013).....	77
Fig 5.1(b): Model II Oral Airway Deposition Fraction for 15L/min	80
Fig 5.1(c): Model II Particle Deposition Pattern	81
Fig 5.1(d): Model II Oral Airway Deposition Fraction for 30L/min	82
Fig 5.1(e): Model II Oral Airway Deposition Fraction for 60L/min.....	83

ABBREVIATIONS AND SYMBOLS

Re	Reynolds Number
Q_{in}	Inlet Volume Flow Rate
DE	Deposition Efficiency
CF-PD	Computational Fluid Particle Dynamics
v	Velocity
ρ	Density
p	Pressure
ν	Kinematic Viscosity
k_T	Turbulent Kinetic Energy
k_L	Laminar Kinetic Energy
ω	Pseudo- Vorticity
ε	Isotropic Dissipation
d_p	Particle Diameter
m_p	Particle Mass
v_p	Particle Velocity
F_p	Particle Forces
Re_p	Particle Reynolds Number

g	Gravitational Acceleration
C_D	Drag Coefficient
DF	Deposition Fraction
Y	Mass Coefficient
D_p	Stokes-Einstein Diffusion Coefficient
F_D	Drag Force
v_{rel}	Particle-Fluid Relative Velocity
A_p	Particle Cross-Sectional Area
μ	Dynamic Viscosity
F_g	Gravitational Force
F_{PG}	Particle Gradient Force
F_l	Lift Force
Cl	Lift Coefficient
V_p	Volume of Particle
VT	Tidal Volume
St	Stokes Number
D_1	Parent Tube Diameter
U	Average Inlet Velocity

I	Turbulence Intensity
F_{rad}	Radial Force
$vratio$	Ratio of total lung volume to be simulated to 3000ml
$qratio$	Ratio of tidal volume to be simulated to 500ml
$ratio$	Ratio of average inspiratory flow rate to be simulated to 15L/min

CHAPTER 1

INTRODUCTION AND OVERVIEW

1.1 Research Motivation

Both health-risk assessment and drug-aerosol therapy of inhaled particulate matter require detailed information on local deposition patterns in the human respiratory tract. Experimental observations are limited to determining total particle deposition or regional particle deposition, the latter with lower accuracy. Also, experimental data sets refer to specific human subjects and inhalation conditions, such as lung volume, breathing pattern and particle size. However, particle depositions are needed for population groups ranging from children to the elderly, where experimental studies are forbidden due to ethical reasons or due to health concerns. Thus, computational particle deposition modeling has become a necessity.

Computational Fluid-Particle Dynamics (CF-PD) is now being extensively used to solve the equations governing the airflow field and particle transport/deposition. There are several commercial software-packages available that can perform these tasks, but they are expensive and quite rigid. In contrast, OpenFOAM is an open-source CFD toolbox provides an option to drastically cut down the cost involved in computer modeling and simulation.

1.2 Research Objectives

Setting up and using OpenFOAM modules, this thesis deals with the modeling and simulation of the airflow as well as microsphere transport and deposition in a representative symmetric geometry of the human tracheobronchial tree and a patient-specific geometry as well as a one-dimensional human-airway trumpet model. The major research objectives were as follows:

- a.) Develop simulation model using OpenFOAM to calculate steady-state airflow structure and microsphere deposition in different airway models.
- b.) Develop radial force correlation and simulation model for one-dimensional trumpet model geometry to calculate microsphere deposition using OpenFOAM
- c.) Develop simulation model using OpenFOAM to calculate transient air-flow structure and microsphere deposition in different airway models.
- d.) Compare the performance of both CFX (Ansys, Inc.) and OpenFOAM, in terms of accuracy and run-time, by performing simulations to calculate steady and transient airflow fields in a single bifurcation model.

1.3 Basic Human Lung Morphology

The lung is similar to a tree. The structure of a tree comprises of bark, branches and leaves. The airways (trachea, bronchi, and bronchioles) are analogous to the bark and branches of the tree and the air-sacs or alveoli are analogous to the leaves of the tree. Like the tree, the branches of the lung have thick walls, and the alveoli have thin walls. Also like the tree, the thickness of the airway gets thinner and thinner as they approach the alveoli. The surface area of the upper branching system is small compared to the gas-exchange surface, i.e., the alveolar region. Air enters through the mouth or nose, then passes through: the pharynx (the throat), the larynx (the voice box), and the trachea (the wind pipe). The trachea splits to form two bronchi each of which feed air to one of the lung lobes. Each bronchus splits to form bronchioles, which, in turn, split to form smaller bronchioles, and so on. Bronchioles extend about 16 levels of branching to reach the terminal bronchioles. After the terminal bronchioles there are several

generations of respiratory bronchioles, alveolar ducts and alveolar sacs, which collectively are known as the acinus. Acinus is the region where O₂-CO₂ exchange occurs. The airways, other than the acinus, have a mucous layer over the ciliated epithelium. The mucus layer composed of a sole phase of low viscosity (hypo-phase) in which the cilia beat, and a blanket of an overlaying gel phase of high viscosity (epi-phase) which is thought to be moved by ciliary motion towards the pharynx.

Alveoli are the smallest unit in the lung, and there are approximately 300 million of them in each lung. Although alveoli are tiny structures, they have a very large surface area in total (~100 m²) for performing efficient gas exchange. The lungs are supplied by three pulmonary arteries and drained by the pulmonary veins. The smallest units of the pulmonary vasculature are the pulmonary capillaries. The blood barrier between the alveolar space and the pulmonary capillaries is a very thin layer of tissue, consisting of capillary endothelial cells, basement membrane, and airway epithelial cells. This thin layer easily allows rapid gas exchange. During inspiration, oxygen diffuses through the alveoli walls and the interstitial space, into the blood. Carbon dioxide diffuses in the opposite direction during exhalation.

1.4 Literature Review

1.4.1 Geometrical Lung Models

Geometrical human lung models can be grouped into two categories:

a.) Idealized Lung Configurations

Over the years many geometric lung models have been proposed. For experimental studies and computational analyses the respiratory tract has been traditionally segmented into the nasal

cavities, oral airways (i.e., mouth to trachea), the tracheobronchial tree (typically Generations 0-3 or 6) and a part of the alveolar region ranging from single alveolar cells to alveolated ducts. Historically, Weibel (1963) was the first to provide idealized geometric data, i.e., tube diameter and length of symmetrically bifurcating lung airways known world-wide as the Weibel Type A model. It assumes that each lung generation branches symmetrically into two identical daughter branches. This is not realistic. In addition, the configuration and geometric data were based on healthy adult lungs. Children and adult patients with asthma, chronic obstructive pulmonary disease (COPD) or other lung diseases might feature some other unusual pattern in terms of airway geometry. Therefore, various geometric improvements and extensions have been proposed (see Finlay, 2001, Haefeli-Bleuer & Weibel 1988, Horsfield et al. 1971, Phalen et al. 1985, Raabe et al. 1976). In the measurements of Raabe et al.(1976), the structural parameters of the bronchial tree, i.e., diameters, lengths, branching and gravity angles, were recorded for the trachea and all bronchial airways down to about generation 10 but only 10-25% of the bronchiolar airways ending at terminal bronchioles were measured. Based on the measurements of Raabe et al (1976), Yeh and Schum (1980) proposed a deterministic five-lobe typical path model with variable path lengths among the five lobes, but symmetric branching in each lobe. Recently, efforts have been made to develop stochastic lung models (Yu et al.1979, Yu and Diu et al.1982, and Goo and Kim 2003) that offer the possibility to extend the measured data for the specific lungs analyzed by Weibel (1963) or Raabe et al.(1976) to a population at large.

b.) Realistic Airway Models

Because of the shortcomings of idealized lung-airway geometries and the dire need for accurately predicting toxic or therapeutic aerosol depositions, researchers now focus on anatomically based human airway models. Specifically, modern imaging techniques and geometry-file conversion software allow for the representation of patient-specific airway configurations.

In order to generate patient-specific geometries, first the CT-scan images of a subject's respiratory tract (i.e., DiCom files), enhanced with a contrasting agent have to be obtained from a radiologist. The DiCom files are then loaded into the geometry-file-conversion software, such as Mimics/Geomagic (Materialise, Belgium) or Simpleware (Simpleware Ltd., Exeter, UK). It enables the modeler to edit images, isolate the structures of interest and generate 3-D geometry models. The CAD-like geometries are then exported in suitable formats, typically as STL-files to CFD software, for numerical fluid flow and solid structure analysis.

1.4.2 Airflow Structures

The understanding of airflow fields in the human airways is very important for calculating particle transport and deposition. Detailed investigations, both experimentally and theoretically, were recently provided by Lieber and Zhao (1998), Zhang and Kleinstreuer (2002) and Zhang and Kleinstreuer (2004), Kleinstreuer and Zhang (2003a), Shi et al. (2006), and Adler and Brucker (2007). So far, experimental and computational analyses focused mainly on isolated sections of the human airways and mainly for laminar airflow. However, at moderate to high breathing rates the airflow from the larynx to generation G3 is

transitional-to-turbulent which may complicate flow structures as well as aerosol transport and deposition (Kleinstreuer and Zhang, 2003a and Zhang and Kleinstreuer, 2004). Usually, the turbulent intensity in the oral airway rises rapidly after the constriction caused by the soft palate, and then decreases until the disturbance is activated again by the throat (glottis) (Zhang and Kleinstreuer, 2003a and Lin et al., 2007). Turbulence levels seem to increase quickly through the strong varying diameter-zone after the glottis, and then decay approaching an asymptotic level at six-diameter station from the throat (Corcoran and Chigier, 2000). The flow instabilities may be induced again at the bifurcation region due to the great geometric transition from the parent tube to two daughter tubes, while the strongest turbulence fluctuations occur just around the flow dividers due to the contraction of top and bottom surfaces in the carinal ridges (Zhang and Kleinstreuer, 2004). Then, turbulence decays rapidly in the straight segments of the bifurcating tubes. Generally, turbulence which occurs after the throat can propagate to at least a few generations even at a low local Reynolds number (say, $Re = 700$) because of the enhancement of flow instabilities just upstream of the flow divider (Olson et al., 1973 and Zhang and Kleinstreuer, 2004).

Flow in the bronchial segment can be compared with that of flow in bifurcating tubes. In case of inhalation the air stream splits at the flow dividers and new boundary layers are generated at the inner walls of daughter tubes where the maximum velocity stays near the inner wall. The velocity patterns vary with the development of upstream flows and the generation of the new boundary layers near the inner walls at the dividers. The skewed profile with a maximum axial velocity near the inner wall may be observed just after the flow divider as the air streams are

deflected and secondary motions (vortices) are formed because of the centrifugally induced pressure gradient in the normal direction that drives the slower moving fluid from the outside wall towards the inside wall, while the faster moving fluid around the top of the tube is swept outside. Flow during the expiratory phase through the bifurcation is quite different from inspiratory flow. Instead of the air streams being split at each flow divider, two streams come together from the daughter tubes, so that near the flow divider the velocity distributions in the bifurcation plane have indentations at the centers. Velocity profiles with double peaks appear after the flow dividers, but they soon transform into marked centerline velocity peaks because of merging boundary layers. Especially for the high Reynolds number case, a distinct velocity spike at the centerline can be generated.

In case of cyclic inhalation flows, there are two phases of airflow, i.e., accelerating phase and decelerating phase. At the same flow rate, some subtle differences can be observed because of the transient fluid inertia, while the basic flow features remain as described in above paragraph for inspiratory flow. Both the magnitude and velocities during flow deceleration are higher than those at acceleration for the same flow rate. This may be due to lingering effects of zero flow before acceleration and peak flow before deceleration (Zhang et al., 2002).

In this work both planar and non-planar geometries are considered; although, most bifurcations are asymmetric and non-planar. Some studies (Chang 1989, Liu et al., 2003) have shown that inspiratory flow in an asymmetric bifurcation exhibits the main features of the symmetric case. Non-planar geometries only influence the flow in downstream bifurcations (Caro et al 2002, Zhang and Kleinstreuer 2002). For inspiration, the air and particle flow fields in the non-planar

configuration resemble those in the planar configuration, but rotated to some degree and merged with the symmetric secondary vortices (Zhang and Kleinstreuer 2002).

1.4.3 Particle Deposition

Inhaled micron-particle depositions for dosimetry-and-health-risk assessments have been studied for decades. Clearly, the experimental and computational contributions reviewed deal with spherical micron particles. The *in vitro* experimental studies of micron-particle deposition in tracheobronchial airways focused on steady inhalation in glass or metal casts of the TB tree from one to several bifurcations (Oldham et al., 2000, Kim and Fisher, 1999 and Zhang and Finlay, 2005), or realistic airway replica based on cadavers representing trachea (G0) to generations G3, G4 or G5 (see Schlesinger and Lippmann, 1972 and Zhou and Cheng, 2005; among others). The deposition efficiencies at each generation were usually measured in these studies for different combinations of particle size and inspiratory flow rate. However, detailed air/particle transport phenomena as well as local deposition patterns and surface densities of deposited particle in bifurcating airways are difficult to obtain experimentally. Kim and Fisher (1999) used two sequential bifurcation glass tube models, one in -plane (Model A) and a second one in which the second bifurcation was 90 degrees out of plane w.r.t the first bifurcation. The dimensions of the geometry resembled a 3rd-5th generation human bronchial tree. They showed that deposition efficiencies (DE) increased in each bifurcation as a function of increasing Stokes number. In case of symmetric flows, DE was somewhat smaller in the second bifurcation when compared to the first bifurcation in each model. Also, the DE at the first bifurcation was the same in case of both models, but was a little higher in the second

model in the second bifurcation. Their analysis of deposition patterns showed that there were highly localized depositions at bifurcation ridges, irrespective of bifurcation geometry or flow distribution. Similar observations were made by Oldham et al. (2000) but they also developed CF-PD models that agreed well with experimental observation. Cheng et al. published a study in 1999 where they experimentally investigated particle deposition in a realistic human cast replica consisting of oral airway (mouth, pharynx, larynx, and trachea) and three generation of bronchi (G0-G3). Many *in vivo* studies have been conducted with human subjects to calculate total and regional depositions in oral airways and bifurcations (Lippmann, 1977., Foord et al., 1978, Chan and Lippmann., 1980, Emmett et al., 1982, Stahlhofen et al., 1989). In these articles particle deposition was calculated and presented for inlet volumetric flow rates of 15 L/min (resting), 30 L/min(light activity) and 60 L/min (medium activity) in actual human subjects.

Particle deposition takes place mainly due to three phenomena, i.e., inertial impaction, i.e., direct and secondary flows, sedimentation (gravity), and diffusion. In case of micron particles the most predominant mechanism of deposition is inertial impaction, especially around the cranial ridges. Understanding of these phenomena have helped in the development of computer simulation models. Due to the recent advancements in high performance computing technology, many articles have been published which describe the CF-PD modeling for calculating micron particle deposition in representative lung-airway configurations (see Zhang & Kleinstreuer,2002., Zhang & Kleinstreuer 2003., Zhang & Kleinstreuer., 2002, Zhang et al. 2002., Zhang et al. 2008). These articles outline the basic methodologies to calculate airflow

structure and micron particle deposition in ideal bifurcation geometries (Weibel Type A), an idealized human upper airway model and patient-specific geometries. It is assumed in all the above CF-PD based particle deposition articles that the condition of deposition is usually fulfilled when a particle is one radius away from the wall, i.e., it touches an airway surface. The assumption of dilute micron-particle suspensions allows for separate computations of the airflow (Eulerian approach solving the Navier–Stokes equations) and the particle dynamics (Lagrangian approach solving Newton's second law of motion). The same holds for the analysis of submicron particles; however, in that case an Euler–Euler approach is recommended, i.e., the nanoparticle (or vapor) phase is described with the mass transfer equation containing an appropriate diffusion term (Kleinstreuer, 2003 and Zhang et al., 2005). The results calculated in all the above articles matched well with *in vivo* patient-specific deposition data.

CF-PD modeling for calculating particle deposition can be done in both steady and transient flow fields, according to the available experimental data. CF-PD modeling has proven to be a successful technique in predicting particle deposition. It has been established that particle deposition is found to be higher in case of cyclic input waveform than for the steady inhalation waveform. For example, Schlesinger et al. (1982), Gurman et al. (1984), and Kim and Garcia (1991) showed that cyclic inhalation generates higher particle deposition efficiencies than steady inhalation at the mean Reynolds number of the inlet flow waveform. Specifically, Gurman et al. (1984) have estimated a 15% increase in inertial impaction with cyclic flows. Kim and Garcia (1991) calculated that the deposition efficiency (DE) should increase by about

23% with sine-wave type flows regardless of the cyclic frequency. Kim and Garcia (1991) measured the deposition of micron-sized particles in a single bifurcation model approximately representing generations G3–G4 for cyclic flow at mean Reynolds numbers of 679–5547 and Stokes numbers of 0.028–0.25. Their results showed that the DE with cyclic flow was also higher than that obtained with constant flow. It has been shown that the assumption of quasi-steady inhalation is justifiable for micron-particle deposition modeling, when an equivalent inlet Reynolds number is selected. Specifically, Zhang et al. (2002a) showed that such an equivalent dimensionless group is the arithmetic mean of the maximum and mean Reynolds numbers of the given inhalation waveform. For elevated inhalation flow rates, i.e., $Q_{in} > 12$ L/min during exercise, transition to turbulent airflow after the larynx (see Fig. 1.4(a)) may occur with re-laminarization further downstream. It was shown that the Low-Reynolds-Number $k-\omega$ turbulence model of Wilcox (1998) adequately describes these changing flow regimes (Kleinstreuer and Zhang, 2003a, Varghese and Frankel, 2003, Zhang and Kleinstreuer, 2003a). However, later on they documented improvements (Zhang and Kleinstreuer, 2011) when using the SST transition model (Menter et al., 2006) and LES models.

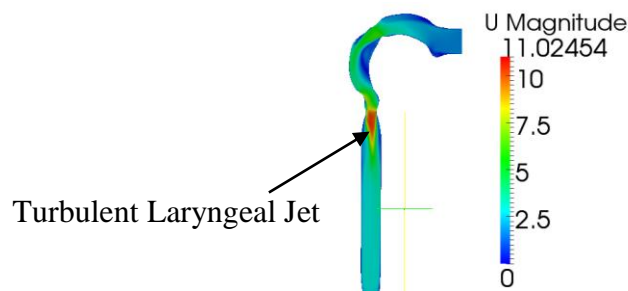


Fig 1.4(a): Velocity Distribution Contours in an Oral Airway Model

CHAPTER 2

FLUID FLOW AND PARTICLE TRANSPORT

2.1 Fluid Flow Equations

For the validation cases involving laminar incompressible airflow, the describing equations are as follows:

Continuum:

$$\nabla \bullet \mathbf{v} = 0 \dots\dots\dots (1)$$

Momentum:

$$\frac{\partial \mathbf{v}}{\partial t} + (\nabla \bullet \mathbf{v})\mathbf{v} = -\frac{1}{\rho} \nabla p + \nabla \bullet [v(\nabla \mathbf{v} + (\nabla \mathbf{v})^T)] \dots\dots\dots (2)$$

where \mathbf{v} is the fluid velocity vector; ρ is the fluid density; p is the pressure, ν is the fluid kinematic viscosity, and $()^T$ represents the transpose of $\nabla \mathbf{v}$. The above equations are discretized and solved on a computational mesh representing the target geometry (see Fig. 3.2(a)).

As mentioned in Section 1.4.3, at moderate to high breathing rates, i.e., $Q_{in} > 12$ L/min, the airflow from the larynx to generation G3 is transitional-to-turbulent which may complicate flow structures as well as aerosol transport and deposition (Kleinstreuer and Zhang, 2003a and Zhang and Kleinstreuer, 2004). It was shown (Zhang and Kleinstreuer, 2011) that SST transition model and LRN $k-\omega$ model are suitable for modeling transitional turbulent behavior in airway models. In this study a new transitional turbulence model, the *kkLOmega* model (Walters and Cokljat, 2008), is used to simulate transitional and turbulent effects. This model is based on the basic framework of the $k-\omega$ model but is adapted to capture the

transitional effects as well. In addition to the Navier-Stokes equations, three additional transport equations are solved, i.e., for the turbulent kinetic energy (k_T), laminar kinetic energy (k_L) and scale determining factor (ω), defined as $\omega = \frac{\varepsilon}{k_T}$, where ε is the isotropic dissipation. The mathematical modeling details along with model equations and parameters can be found in Appendix A, based on the paper by Walter and Cokljat (2008).

2.2 Particle Transport

As described in Section 1.4.3, particle deposition takes place mainly due to three phenomena, i.e., inertial impaction which includes direct and secondary flows, sedimentation (gravity), and diffusion. In case of micron-size particles ($d_p \geq 1 \mu\text{m}$), the Euler-Lagrange particle tracking approach is adopted. In this case, particles are treated as a discrete phase whose motion is affected by fluid flow and particle inertia is taken into account. For dilute particle suspensions any influence of the particles on the fluid flow field can be neglected. Particle trajectories are governed by Newton's Second Law:

$$m_p \frac{d\vec{v}_p}{dt} = \sum \vec{F}_p \dots\dots\dots (3)$$

where m_p is the mass of a single spherical particle, d_p is the particle diameter and $\sum \vec{F}_p$ are the forces acting on it. In light of small particle Reynolds numbers, $\text{Re}_p \sim |\vec{v} - \vec{v}_p| \ll 1$, a large density ratio, $\rho_p / \rho \gg 1$, and $d_p > 1 \mu\text{m}$, most of the known particle forces can be discounted using order of magnitude arguments. First these particles are relatively large, so Brownian

motion can be neglected. Second, the particulate material considered is far denser than air, causing terms that depend on the density ratio, such as pressure force, buoyancy force, virtual mass effect and Basset force, to be very small. Third, the lift forces in the present Stokes flow limit are negligible because of lack of measurable particle spin (Magnus lift) and the laminar, low-level fluid shear lift (Saffman lift). Longest, Kleinstreuer, and Buchanan (2001) confirmed these last two assumptions in evaluating the impact of several near-wall force terms for blood particle flow, including the Saffman lift, by comparison with experimental observations. The resulting, simplified particle equation of motion, i.e., Eq. (4), which produced excellent particle deposition results when compared with measurements (Kim and Fisher, 1999; and Oldham et al., 2000), will make it easy to elucidate the physical processes at work. Hence, the final equation can be stated as:

$$\frac{d}{dt}(m_p v_p) = \frac{1}{8} \pi \rho d_p^2 C_{D_p} (v - v_p) |v - v_p| + m_p g \dots\dots\dots (4)$$

where ρ is the air density; v_p , m_p and d_p are the velocity, mass and diameter of the particle, respectively; g is the gravitational acceleration and C_D is the drag coefficient described in Section 2.3.1. The regional deposition of micron particles in human airways can be quantified in terms of the deposition fraction (DF) or deposition efficiency (DE) in a specific region (e.g. oral airway, first second and third bifurcation, etc.). They are defined as follows:

$$DF_{\text{particle}} = \frac{\text{Number of deposited particles in a specific region}}{\text{Number of particles entering the mouth}} \dots\dots\dots (5)$$

$$DE_{\text{particle}} = \frac{\text{Number of deposited particles in a specific region}}{\text{Number of particles entering this region}} \dots\dots\dots (6)$$

In case of spherical nanoparticles ($d_p < 100\text{nm}$) the Euler-Euler modeling approach is adopted. This approach treats the particle as a continuum field, and neglects the particle inertia and the effects of the particle phase on the flow field. In this model the particle concentration is calculated from a convective-diffusive equation using terminal particle velocity. Ignoring coagulation, surface growth, nucleation, and other internal/external forces, the convection-diffusion mass transfer equation of nanoparticles can be written as:

$$\frac{\partial Y}{\partial t} + \frac{\partial}{\partial x_j} (u_j Y) = \frac{\partial}{\partial x_j} [D_p \frac{\partial Y}{\partial x_j}] \dots\dots\dots (7)$$

where x_j is the coordinate variables ($j = 1, 2, 3$), u_j is the air velocity, Y is the mass fraction, and D_p is the Stokes-Einstein diffusion coefficient.

The local mass flux of the nanoparticles can be determined as:

$$m_w = \rho A_i j_{\text{wall},i} \dots\dots\dots (8)$$

where ρ is the gas mixture density, A_i is the area of local wall cell (i) and $j_{\text{wall},i}$ is the particle flux at the local wall cell given by:

$$j_{\text{wall},i} = -D_p \frac{\partial Y}{\partial n} \Big|_{\text{wall},i} \dots\dots\dots (9)$$

The regional DF and DE can be determined as:

$$DF_{\text{region}} = \frac{\sum_{i=1}^n (A_i j_{\text{wall},i})}{(Q_{\text{mouthin}} Y_{\text{mouthin}})} \dots\dots\dots (10)$$

$$DE_{region} = \frac{\sum_{i=1}^n (A_i j_{wall,i})}{(Q_{localin} Y_{localin})} \dots\dots\dots (11)$$

where n is the number of wall cells in one specific airway region. The subscript “*mouthin*” refers to mouth inlet, while “*localin*” refers to the inlet at the specific airway generation. The local inlet flow rate and particle mass are calculated as the sum of local values of cells at this specific inlet.

2.3 Particle Interactions

There are various forms of (solid) particle interactions causing up to four-way coupling phenomena:

- particle-particle and particle-fluid interactions influencing individual particle trajectories and fluid flow between neighboring particles, respectively;
- particle-wall interactions such as direct impacting, interception, bouncing, rolling, and repercussion;
- random inter-particle collisions resulting in Brownian-type motion for submicron particles, or particle aggregation/droplet coalescence, or a drift flux, or an apparent viscosity of the particle phase; and
- fluid-particle interactions as expressed with Newton’s second law of motion, or with dispersion terms in the enhanced mass transfer equation, as well as turbulence modulation in dense particle suspensions.

In the current study fluid-particle interaction, as expressed with Newton’s second law of motion, and particle-wall interaction have been considered, while the other interactions were neglected. It has been observed during the course of this study that considering only fluid-particle interaction and particle-wall interaction in case of micron-size particles yields reasonably good results when compared to experimental data. This saves computational time and resources that would have been spent in solving additional interaction equations or complicated terms. Particles are assumed to stick to the wall when they are one radius away from that surface.

2.4 Particle Forces

A solid particle experiences a number of forces in a fluid flow field. Depending upon the size and way the experiments are performed, one has to consider relevant forces in order to develop successful simulation models. The following forces have been considered for microspheres:

1.) Drag Force

It is the force that is experienced by the solid particle opposite to its relative motion with respect to fluid flow. It is given by the following mathematical expression:

$$F_D = \frac{1}{2} \rho (v_{rel})^2 C_D A_p \dots\dots\dots (12)$$

Here ρ is the density of fluid, v_{rel} is the relative velocity of solid particle with respect to the fluid phase, C_D is the drag coefficient and A_p is cross sectional area given by $\frac{\pi d_p^2}{4}$ in case of microspheres. This forces acts in a direction opposite to the direction of v_{rel} .

There are available mathematical models for determining C_D for spherical particles, which were obtained experimentally. The drag model implemented in OpenFOAM-2.1.1 can be presented as:

$$C_D = \left\{ \begin{array}{ll} \frac{24}{\text{Re}_p} (1 + 0.15 \text{Re}_p) & 0 \leq \text{Re}_p \leq 1000 \\ 0.424 & \text{Re}_p > 1000 \end{array} \right\} \dots\dots\dots (13)$$

where Re_p is the particle Reynolds number, defined as:

$$\text{Re}_p = \frac{\rho |\vec{v} - \vec{v}_p| d_p}{\mu} \dots\dots\dots (14)$$

where μ is the fluid viscosity.

2.) Gravitational & Buoyancy Forces

The gravitational force is due to acceleration because of gravity that particles experience. This force is responsible for the deposition of particle due to sedimentation. It is simply implemented as:

$$\vec{F}_g = m_p \vec{g} \dots\dots\dots (15)$$

where m_p is the mass of solid spherical particle and \vec{g} is the acceleration vector due to gravity.

Care should be taken in applying gravitational force in appropriate direction, as per the experimental set up, to avoid erroneous results.

The buoyancy force is the force exerted by the fluid on an immersed object such that it opposes

the weight of the object. This force is caused by the hydrostatic pressure difference created across the object in a fluid.

In OpenFOAM selecting gravitational force model automatically takes into account the buoyancy force. The exact mathematical form in which both the forces are implemented in OpenFOAM is as follows:

$$\vec{F}_g = m_p g \left(1 - \frac{\rho}{\rho_p}\right) \dots\dots\dots (16)$$

3.) Pressure Gradient Force:

This force can be understood as the force required to accelerate the fluid which could occupy the space if the particle were absent. The pressure gradient force results from the local fluid pressure gradient around the particle and is defined as:

$$F_{PG} = -V_p \nabla p \dots\dots\dots (17)$$

where V_p is the volume of the solid particle. This force is applied on the particle in the direction of the pressure gradient.

This force is only important if large fluid pressure gradients exist and if the particle density is smaller than or similar to the fluid density. Neglecting diffusive and source terms in the momentum equation, the pressure gradient can be replaced by the velocity gradient. Assuming constant fluid density, the pressure gradient force can be written as:

$$\vec{F}_{PG} = \frac{m_p}{\rho_p} \rho \left[(\vec{v} \bullet \nabla) \vec{v} + \frac{\partial \vec{v}}{\partial t} \right] \dots\dots\dots (18)$$

Here m_p refers to the particle mass and ρ_p is the particle density.

4.) Lift Force:

The lift force is the component of aerodynamic force that acts in a direction perpendicular to that of the drag force. For calculating the lift force on spherical solid particles, and it could be applied to liquid drops that are not significantly distorted, Saffman-Mei model (Mei & Klausner, 1994) is found to be suitable. It is a generalization of the older Saffman model (Saffman 1968), which was applicable to a lower range of particle Reynolds numbers than the Saffman-Mei model.

$$\vec{F}_l = \frac{m_p}{\rho_p} \frac{d_p}{2} \rho C_l (\vec{v} - \vec{v}_p) \times (\nabla \times \vec{v}) \dots\dots\dots (19)$$

In the above equation (Mei and Klausner, 1994), C_l is the lift coefficient which is given as:

$$C_l = \frac{3}{2\pi\sqrt{Re_\omega}} C_{l_d} \dots\dots\dots (20)$$

$$C_{l_d} = \begin{cases} 6.46f & Re_p < 40 \\ 6.46 * 0.0524 \sqrt{\beta} Re_p & Re_p \geq 40 \end{cases} \dots\dots\dots (21)$$

$$f = (1 - \alpha) * e^{(-0.1 * Re_p)} + \alpha \dots\dots\dots (22)$$

$$\alpha = 0.3314 * \sqrt{\beta} \dots\dots\dots (23)$$

$$\beta = 0.5 * \frac{Re_\omega}{Re_p} \dots\dots\dots (24)$$

$$Re_\omega = \frac{\rho |\nabla \times \vec{v}| d_p^2}{\mu} \dots\dots\dots (25)$$

2.5 Particle Deposition Mechanism

There are three deposition mechanisms that are responsible for particle deposition, i.e., inertial impaction, gravitational sedimentation, and diffusion. Although deposition takes place by the combined forces exerted by these mechanisms, only one or two mechanisms usually play a dominant role for a given inhalation condition and the region of respiratory tract where the particles are present. Deposition of particles also depends on the particle characteristics (e.g., size, shape and density) but also on the subject's breathing pattern, which determines the mean residence time of an inspired aerosol in the respiratory tract and the mean volumetric flow rate. Usually deposition is given as a function of the particle diameter, however, any statement about deposition is incomplete without mentioning the particle density and breathing pattern for which these deposition data were obtained. Deposition also depends on the morphology of the respiratory tract and on the distribution of inspired aerosols in the lungs. The influence of these factors upon deposition can be studied in subjects inhaling the same aerosol under the same breathing conditions.

Inertial impaction refers to the phenomenon in which particles strike the surface of the respiratory system and stick. This kind of phenomenon is mainly responsible for microsphere deposition at the tongue portion in the oral cavity, the outer bend of the pharynx/larynx and the regions just upstream of the glottis and the straight tracheal tube. Then impaction occurs at the airway bifurcation points, i.e., the carinal ridges. In general, when microspheres enter the respiratory tract they first experience inertial transport.

As they penetrate further into the respiratory tract, the efficacy of this transport may diminish

and the efficacy of gravitational transport is enhanced. This is due to the fluid dynamics of the respiratory tract. An inspired aerosol flows through the upper respiratory tract at high velocity and only remains in this region for a short period, so that particle deposition is governed by inertial impaction. On the other hand, the long residence time of the aerosol in the lower respiratory tract is associated with a low velocity, so that particle deposition is governed by gravitational sedimentation. Consequently, with increasing particle size, the site of deposition is shifted from the lower to the upper respiratory tract. In the bronchial region, particle deposition during inspiration is due to inertial impaction in the upper airways and due to gravitational sedimentation in the lower airways during expiration it is only due to gravitational sedimentation in the lower airways.

Diffusion remains as a dominant mechanism for particles as large as $d_p = 0.5 \mu\text{m}$ and its influence stretches to $d_p = 3\text{--}5 \mu\text{m}$, particularly in the alveolar region where $\text{Re} < 1$. Although effects of sedimentation are noticeable for submicron particles ($0.1 \mu\text{m} < d_p < 1 \mu\text{m}$), sedimentation plays a major role in deposition of micrometer size particles ($1 \mu\text{m} < d_p < 7 \mu\text{m}$) with its peak effect at $d_p = 4\text{--}7 \mu\text{m}$ (Kim et al., 2007). In the alveolar region sedimentation is the dominant mechanism for deposition of particles with $d_p > 1 \mu\text{m}$.

The predominant mechanism of deposition for particles smaller than about 500 nm is diffusion (Schulz et al., 2000). The probability of deposition by diffusion increases as the particle size decreases (Stuart, 1973; Kim, 2000). In comparison with larger particles, diffusional deposition should be

favored in the distal airways and alveoli because reduced airflow increases residence time in these regions. Therefore, distal respiratory deposition of Ultra-Fine Particles (UFP) in the range of 20 to 40 nm would be expected to exceed that of larger particles.

Breathing patterns also effect particle deposition. During controlled breathing experiments in a laboratory setting, increasing tidal volume (VT) with flow rates held constant increases deposition for all respirable particles, and increasing flow rates with tidal volume held constant decreases diffusional deposition. Studies of the deposition of 1000- to 5000-nm particles (reviewed in Schulz et al., 2000) have shown either increases or no change with exercise. During exercise, tidal volume increases to a greater degree than respiratory rate, which may favor diffusional deposition mechanisms. Determining the influence of exercise on UFP deposition is important in understanding UFP dosimetry, because particle intake rates may be increased more than six- to eightfold during exercise on the basis of increased minute ventilation alone. Children and adults exercising outdoors may therefore be at increased risk for adverse health effects from UFP exposure (Dockery et al., 1989).

CHAPTER 3

OpenFOAM® SOFTWARE USE AND COMPUTER MODEL VALIDATIONS

3.1 OpenFOAM

3.1.1 Introduction and Overview

The OpenFOAM® (Open Field Operation and Manipulation) CFD Toolbox is a free, open-source CFD software package which has a large user base across most areas of engineering and science, from both commercial and academic organizations. OpenFOAM has an extensive range of features to solve anything from complex fluid flows involving chemical reactions, turbulence and heat transfer, to solid dynamics and electromagnetics. It includes tools for meshing, notably *snappyHexMesh*, a parallelized mesher for complex CAD geometries, and for pre- and post-processing. Almost everything (including meshing, and pre- and post-processing) runs in parallel as standard, enabling users to take full advantage of computer hardware at their disposal.

By being open, OpenFOAM offers users complete freedom to customize and extend its existing functionality, either by themselves or through support from OpenCFD. It follows a highly modular code design in which collections of functionality (e.g. numerical methods, meshing, physical models, etc.) are each compiled into their own shared library. Executable applications are then created that are simply linked to the library functionality. OpenFOAM includes over 80 solver applications that simulate specific problems in engineering mechanics and over 170 utility applications that perform pre- and post-processing tasks, e.g., meshing, decomposition of case for parallel processing, mesh manipulation, data visualization, etc.

3.1.2 Mesh Generation

Mesh generation for OpenFOAM can be done in two ways:

- 1.) External Mesh Generators: OpenFOAM accepts meshes generated by any of the major mesh generators and CAD systems. In OpenFOAM, mesh conversion process is accomplished by going inside the case directory and giving mesh conversion commands listed in Table 3.1 followed by the mesh name. For example, if a mesh is available in Fluent format, say 'fluent.msh', then it can be converted by accessing the OpenFOAM case directory, where this mesh is also saved, and execute it with the command:

```
fluent3DMeshToFoam fluent.msh
```

Here `fluent3DMeshToFoam` is a OpenFOAM utility command that converts any mesh in Fluent format to OpenFOAM format, and `fluent.msh` is file name of the mesh in Fluent.

Table 3.1: List of OpenFOAM mesh converter commands

Command	Function
<i>ansysToFoam</i>	Converts an <i>ANSYS</i> input mesh file, exported from <i>I-DEAS</i> , to OPENFOAM® format
<i>cfx4ToFoam</i>	Converts a <i>CFX 4</i> mesh to OPENFOAM® format
<i>datToFoam</i>	Reads in a <i>datToFoam</i> mesh file and outputs a point file. Used in conjunction with <i>blockMesh</i>
<i>fluentMeshToFoam</i>	Converts a <i>Fluent</i> mesh to OPENFOAM® format

Table 3.1: Continued

<i>gmshToFoam</i>	Reads .msh file as written by Gmsh
<i>gambitToFoam</i>	Converts a <i>GAMBIT</i> mesh to OPENFOAM® format
<i>star3ToFoam</i>	Converts a <i>STAR-CD</i> (v3) <i>PROSTAR</i> mesh into OPENFOAM® format
<i>star4ToFoam</i>	Converts a <i>STAR-CD</i> (v4) <i>PROSTAR</i> mesh into OPENFOAM® format
<i>tetgenToFoam</i>	Converts .ele and .node and .face files, written by tetgen

2.) *blockMesh* and *snappyHexMesh*: OpenFOAM supports unstructured meshes of cells of any shape; cells in OpenFOAM can have any number of faces, while faces can have any number of edges. Such complete freedom on cell shape gives greater flexibility for the generation of meshes around complex boundaries, embedded refinements, etc. For simple geometric cases OpenFOAM offers *blockMesh*, which is a meshing utility that allows the user to generate basic meshes for those geometries. On the other hand, *snappyHexMesh* offers a meshing utility that covers highly complex CAD surfaces.

a.) *blockMesh*: For simple geometries, there is *blockMesh*, a multi-block mesh generator that generates meshes of hexahedra from a text configuration file. The OpenFOAM distribution contains numerous example configuration files for *blockMesh* to generate meshes for flows around simple geometries, e.g., a cylinder, a wedge, etc.

b.) *snappyHexMesh*: For complex geometries, there is *snappyHexMesh* meshing utility that meshes to surfaces from CAD, but also allows the user to define simple geometric entities such as boxes, spheres, planes, etc. The *snappyHexMesh* utility can run in parallel, so it can generate meshes with 100s of millions of cells, given a sufficient number of CPUs and memory.

For using *snappyHexMesh* first a background mesh has to be generated using *blockMesh* meshing utility, and *snnapyHexMesh* is then used to generate meshes conforming to the surface of complex geometries.

3.1.3 OpenFOAM Solvers

An extensive set of OpenFOAM solvers has evolved (and is still growing) that is available to users. In addition to solving CFD problems, OpenFOAM has also found use in computational application areas such as stress analysis, electromagnetics and finance because it is fundamentally a tool for solving partial differential equations, rather than just a CFD package in the traditional sense. For a complete list of solvers and their description please refer to Appendix B. The solvers used to perform simulations for this study include the following.

a.) *simpleFoam*: This is a very basic steady-state solver that solves the Navier-Stokes equations for incompressible 3D fluid flow. It has an option for including turbulence models. The equations are discretized according to the numerical schemes specified and solved in accordance with the SIMPLE algorithm (Patankar, 1982). The SIMPLE (Semi-Implicit Method for Pressure-Linked Equations) allows to couple the Navier-Stokes equations with an iterative procedure, which can be summed up as follows:

- 1.) Set the boundary conditions.

- 2.) Solve the discretized momentum equation to compute an intermediate velocity field.
- 3.) Compute the mass fluxes at the cell faces.
- 4.) Solve the pressure equation and apply under-relaxation.
- 5.) Correct the mass fluxes at the cell faces.
- 6.) Correct the velocities on the basis of the new pressure field.
- 7.) Update the boundary conditions.
- 8.) Repeat till convergence.

Steps 4 and 5 can be repeated for a prescribed number of times to correct for non-orthogonality.

b.) *pimpleFoam*: This is a transient solver that solves the Navier-Stokes equations for incompressible 3D fluid flow. It has an option to include turbulence models. The equations are discretized according to the numerical schemes specified and solved in accordance with a PISO -SIMPLE algorithm. The PISO-SIMPLE algorithm is a combination of the SIMPLE algorithm described earlier in this section and the PISO (Pressure Implicit with Splitting of Operator) algorithm. It can be summed up as follows:

- 1.) Set the boundary conditions.
- 2.) Solve the discretized momentum equation to compute an intermediate velocity field.
- 3.) Compute the mass fluxes at the cell faces.
- 4.) Solve the pressure equation.
- 5.) Correct the mass fluxes at the cell faces.
- 6.) Correct the velocities on the basis of the new pressure field.
- 7.) Update the boundary conditions.

- 8.) Repeat from Step 3 on for a prescribed number of times.
- 9.) Increase the time step and repeat from Step 1 on.

As already seen for the SIMPLE algorithm, Steps 4 and 5 can be repeated for a prescribed number of times to correct for non-orthogonality.

c.) *icoUncoupledKinematicParcelFoam*: This is a transient Lagrangian particle-tracking solver. In this solver no continuity or momentum equations are solved. The steady-state flow field is calculated using *simpleFoam* for a given computational domain. It provides initial conditions for a given simulation case, employing *icoUncoupledKinematicParcelFoam* for the same computational domain. This solver computes the particle tracks, using Newton's Second Law, by taking into account the particle forces specified in the particle properties file (called *kinematicCloudProperties*).

3.1.4 Post-processing

OpenFOAM provides the following options to post-process results obtained using OpenFOAM solvers:

- a.) *ParaView*

The main post-processing tool provided with OpenFOAM is a reader module to run with ParaView, an open-source, visualization application.

ParaView uses the Visualisation Toolkit (*VTK*) as its data processing and rendering engine and can therefore read any data in *VTK* format. OpenFOAM includes the *foamToVTK* utility to convert data from its native format to *VTK* format, which means that any *VTK*-based graphics tools can be used to post-process OpenFOAM cases. This provides an alternative means for

using *ParaView* with OpenFOAM. Here, *paraFoam* is the name of a script that launches *ParaView* using the reader module supplied with OpenFOAM. It is executed like any of the OpenFOAM utilities by the single command from within the case directory by typing in *paraFoam*.

b.) *Fluent*

It is possible to use *Fluent* as a post-processor for the cases run in OpenFOAM. Two converters are supplied for the purpose: *foamMeshToFluent* which converts the OpenFOAM mesh into *Fluent* format and writes it out as a *.msh* file; and *foamDataToFluent* converts the OpenFOAM results data into a *.dat* file readable by *Fluent*.

Apart from *Paraview* and *Fluent* commercial post-processing software like *EnSight*, *FieldView* can also be used to visualize OpenFOAM results.

3.1.5 Modular OpenFOAM Case Structure

In this section, a general OpenFOAM simulation case setup is described, where the flowchart illustrates the case directory structure:

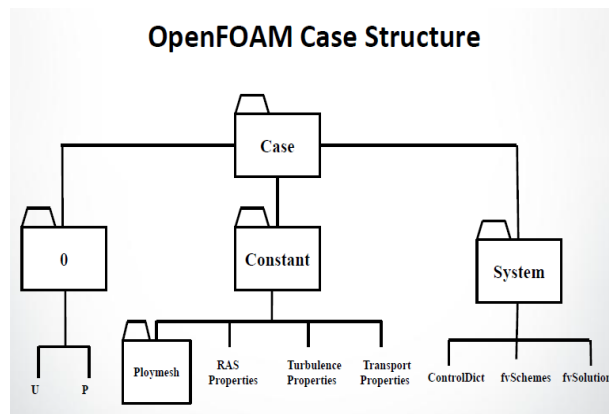


Fig 3.1(a): OpenFOAM Case Structure

Each directory/sub-directory contains the following.

Case: This is the main case directory containing all the sub-directory and relevant case files.

To run a simulation one needs get inside the case directory and type in the solver name.

0: This is the sub-directory that contains the initial and boundary conditions for the fields relevant to the case. In case of basic incompressible laminar fluid flow simulations only velocity (**U**) and pressure(**p**) fields need to be initialized and described at the boundaries. In case of other complicated simulations, involving turbulence, heat transfer and/or chemical reactions, additional boundary conditions may have to be specified.

Constant: This sub-directory contains the mesh and other fluid flow properties, e.g., turbulence model, turbulence properties, transport model, etc. This subdirectory contains another sub-directory called *PolyMesh* that contains the mesh data. Fluid flow properties are specified in text file format as shown in the image (*RAS Properties, Turbulence Properties, Transport Properties*).

System: This sub-directory contains solution control files and parameters. Every OpenFOAM case's system sub-directory contains at least three text files, i.e., *ControlDict*, *fvschemes* and *fvSolution*. In case a simulation is to be run in parallel it contains one more essential file called *decomposeParDict* that specifies the number of processors to be used and each processor's load. There may be more files required to perform other tasks. *ControlDict* file controls input/output operations, *fvschemes* text file contains numerical schemes and *fvSolution* text file contains solution control settings like convergence criteria, relaxation factors, equation solvers, etc.

Once all the required files and directories are set up, the user needs to enter the case directory through the terminal and run the following applications in order:

- 1.) *checkMesh*: This utility is run to see if the mesh is fine. In case the mesh is good a 'Mesh OK' message is displayed.
- 2.) *renumberMesh*: After the *checkMesh* result is found good, *renumberMesh* utility should be run which reduces the bandwidth size and hence reduces the computation time.
- 3.) *decomposePar*: After performing the above two steps if the user wants to run the case in parallel then this application decomposes the case into a number of directories (equal to the number of processors specified). The method of parallel computing used by OpenFOAM is known as domain decomposition, in which the geometry and associated fields are broken into segments and allocated to separate processors for solution. The process of parallel computation involves decomposition of the mesh and fields and running the application in parallel.
- 4.) *solver*: Now the simulation is triggered by typing in the desired solver command. For example, for an incompressible steady-state simulation, the user should type *simpleFoam* or in the case of a transient simulation the user should type *pimpleFoam*. Typing in simply the solver command will trigger the simulation on only one processor. For running the simulation in parallel the following command should be given:

```
mpirun -np 4 simpleFoam -parallel
```

OpenFOAM software is an attractive N-S equation solver, being free of charge, maintaining a large software library and allowing user-supplied module additions via C++

programming. However, once set up it has to be carefully checked for convergence, robustness, ease-of-use, run-time and accuracy before solving a particular CFD problem. In subsequent sections several fluid-particle dynamics cases in bifurcating conduits are analyzed, comparing results from OpenFOAM and CFX (Ansys, Inc., Canonsburg, PA) with experimental observations.

3.2 Case A: Steady-state Airflow Fields

As the particle deposition efficiencies (Des) in this study are all calculated for steady inlet flow rates, first OpenFOAM's steady-state solver was validated against the Zhao and Lieber (1994) experimental results for a symmetric single bifurcation model with constant inlet flow. The numerical results were found to be consistent with experimental data and in-house ANSYS CFX numerical results. The velocity profile in the bifurcation portion were found to be naturally skewed towards the inner wall due to the curvature of the daughter tubes, where centrifugal forces develop secondary flows and hence the velocity profile becomes skewed.

3.2.1 Geometry and Mesh

A single-bifurcation geometry was created for validations in OpenFOAM. The geometrical features were adapted from Zhao and Lieber (1994). Owing to the complexity of generating a representative bifurcation model, the CAD package Solid Works 2010 was used to generate an equivalent three-dimensional surface model as shown in Fig 3.2(a). The diameter (D) of the parent tube was 3.81 cm. The length of the flow divider was calculated from the relation $L=2.5 D$ and the branch angle $2\alpha=70^\circ$. The radius of the daughter tubes were chosen to be $0.714D$, so that the cross-sectional area is conserved at bifurcation. The radius of curvature of the

daughter tube was $7*D/\sqrt{2}$ and the angle β was fixed at 18° .

A high quality mesh was created using ANSYS ICEM CFD 14.0. The mesh independence study indicated that a mesh containing 1.2 million elements gave reasonably accurate results. Tetrahedral elements were used to model the core of bifurcating tube geometry while very dense prism layers were used to capture high gradients near the solid wall boundaries.

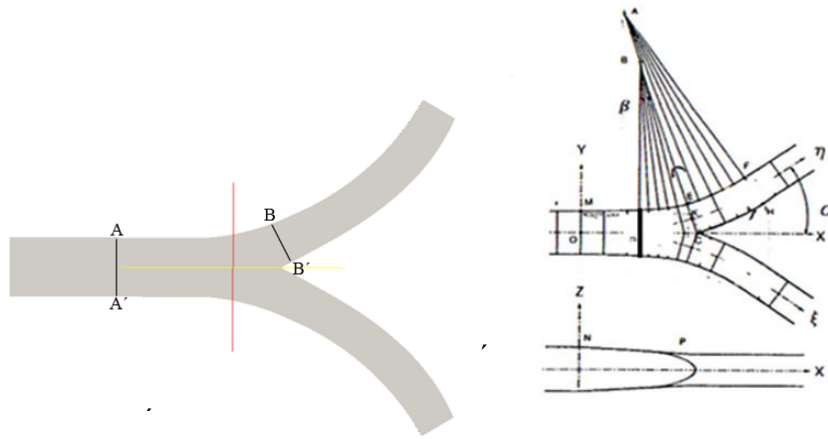


Fig 3.2(a): Case A Geometry

3.2.2 Governing Equations, Boundary Condition and Numerical Schemes

OpenFOAM's *simpleFoam* solver was used to solve the continuity Equation (1) and Navier-Stokes Equation (2) for an incompressible, 3-D, laminar flow under steady-state condition.

A Poiseuille flow profile was specified at the inlet with a Reynolds number equal to 1036. At both the outlets the '*pressureNormalInletOutletVelocity*' velocity boundary condition was specified. This velocity boundary condition is basically a zero gradient condition for velocity

but it keeps the direction of flow normal to the outlet patch. This is similar to the CFX implementation of ‘*opening*’ boundary condition with velocity direction normal to the outlet surface. Pressure at the outlet is kept zero, i.e., a reference value. The no-slip boundary condition was invoked at the walls.

Higher order upwind (linear upwind) scheme and Gauss linear corrected schemes were used to model convective and diffusive terms, respectively.

3.2.3 Results and Discussion

The velocity profiles (Figs. 3.2(b) and 3.2(c)) are in agreement with experimental observations (Zhao and Lieber, 1994), reproducing the skewness of the velocity profiles in the bifurcation towards the inner walls of the daughter vessel. This skewness occurs because of the secondary flow that developed as a result of centrifugal forces around the curved bifurcating portion. Fig 3.2(d) shows that the velocity profiles follow the same trend starting with the parabolic velocity distribution at the inlet and ending with skewed velocity profiles towards the inner wall of the bifurcation.

In Fig. 3.2(b), 3.2(c) OF refers to OpenFOAM simulation data, CFX refers to ANSYS CFX simulation data and EXP is experimental data.

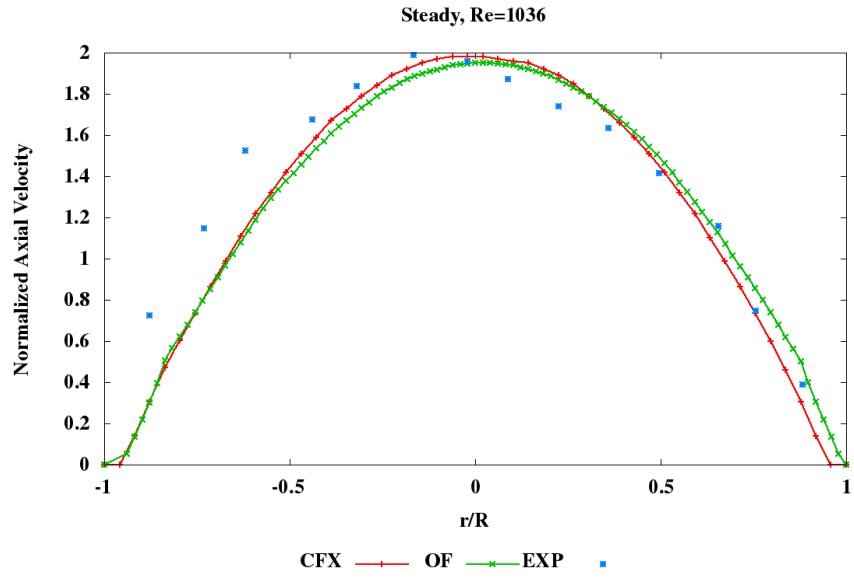


Fig 3.2(b): Case A Velocity Profile at A-A'

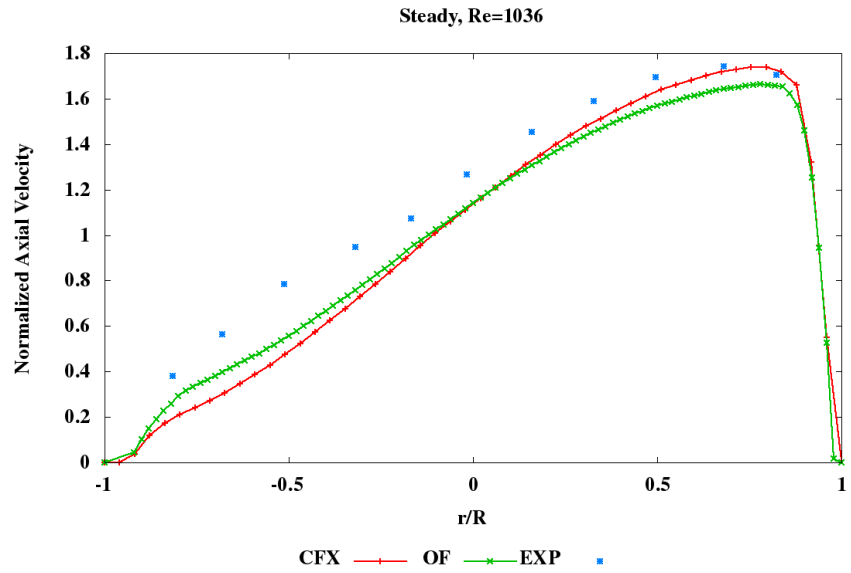


Fig 3.2 (c): Case A Velocity Profile at B-B'

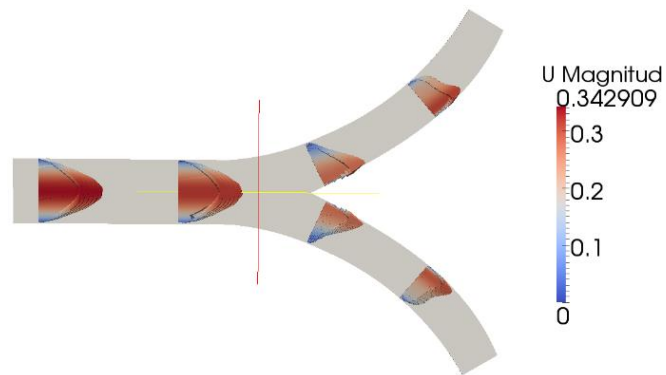


Fig 3.2 (d): Case A Velocity Vector Representation

Flow separation and recirculation regions were not observed at any point inside the bifurcation for any of the Reynolds numbers studied. As the flow proceeds and enters the bifurcation, the effect of geometry become more profound. Secondary flow induced by the curved geometry drives the fluid towards the inner wall of the bifurcation such that the velocity profiles become skewed with the maximum velocity occurring near the inner wall. This skewed velocity profile is typical for the flows in curved pipe (Pedley 1977, Snyder et al. (1985))



Fig 3.2 (e): Case A Probe Location at C-C'

The velocity profile in the transverse plane(3.2(f)) show a little different behavior. As the flow proceeds downstream in the bifurcation plane the velocity profile takes an *M-shape*, i.e., the velocity at the center reduces as compared to the velocity near the wall in the transverse plane. This *M-shape* begins to appear at the station where the bifurcation again becomes straight and the velocity profile in the bifurcation plane starts adjusting back to parabolic profile as there is no radius of curvature in the straight section. The fluid now starts moving to the outer periphery of the bifurcation and takes the momentum away from high speed moving bulk fluid at the center.

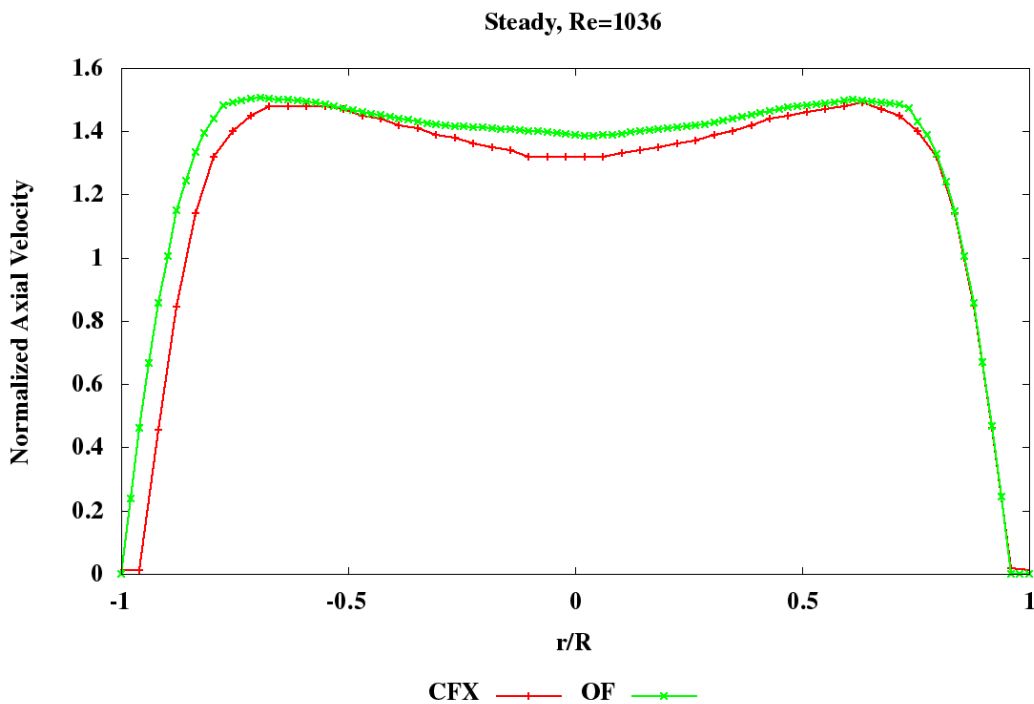


Fig 3.2 (f): Case A Transverse Plane Velocity Profile at C-C'

This results in drop of velocity magnitude at the center resulting in *M-shape* profile. This was confirmed by the simulation results (see Fig 3.2(e) and Fig 3.2(f)).

3.3 Case B: Transient Airflow Fields

In this validation, transient airflow fields were simulated using a geometry that exhibit the same geometrical features as in validation Case A; but, with extended outlets to prevent numerical divergence due to backflow. Symmetry was used to reduce the computation time, as it is high in case of transient simulations. The inlet waveform was taken from Zhao and Lieber (1998). OpenFOAM's transient solver *pimpleFoam* was used to compute the velocity field in space and time in the given geometry.

3.3.1 Governing Equations, Boundary Condition and Numerical Schemes

OpenFOAM's *pimpleFoam* solver was used to solve the continuity Equation (1) and Navier-Stokes Equation (2) for an incompressible, 3-D, laminar flow under transient condition.

Again, a Poiseuille flow profile was specified at the inlet with a peak Reynolds number equal to 2207 ($0 < Re_{in} < 2207$ i.e., no turbulence). At both the outlets the '*pressureNormalInletOutletVelocity*' velocity boundary condition was specified. Pressure at the outlet was kept zero, i.e., a reference value. No-slip boundary condition was invoked at the walls.

Input waveform was given as a sinusoidal expression (Zhang et al. 2002). Figure 3.3(a) represents the input waveform.

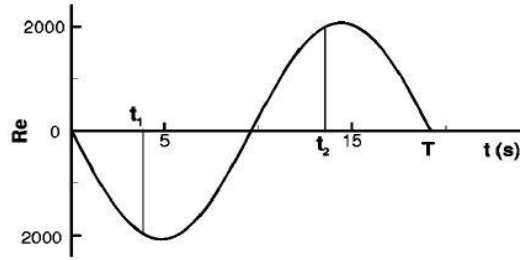


Fig 3.3(a). Case B Input Waveform

This waveform was given as an input to the OpenFOAM solver in form of a Fourier expression obtained by extracting data points from the image, followed by curve-fitting of the obtained data points in form of a Fourier expression, using MATLAB.

Higher order upwind scheme, Gauss linear corrected scheme and Euler backward schemes were used to model convective, diffusive and unsteady terms, respectively.

3.3.2 Results and Discussion

Total time period (T) of one input pulse was approximately 19.2s. The transient simulation results are reported at two time steps, i.e., 0.2T (3.9s) and 0.7T (13.7s). For each time step, results are reported at three stations (2, 10, 15) as shown in Fig. 3.3b.

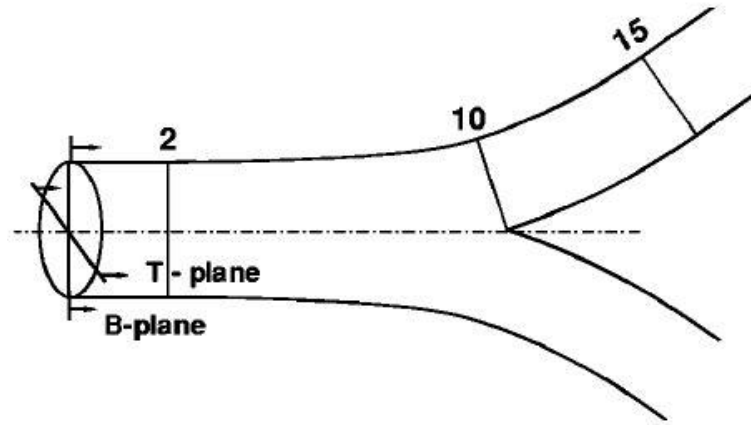


Fig 3.3(b): Case B Probe Locations

Time: 0.2T, Location: Station 2

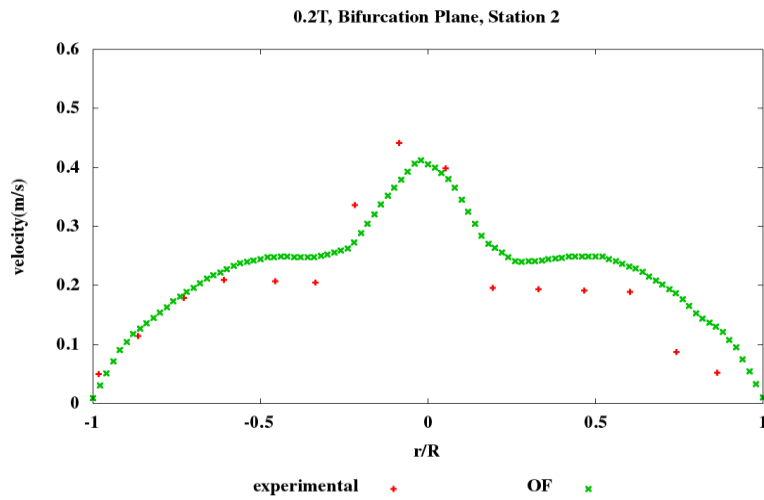


Fig 3.3(c): Case B Velocity Profile at Station 2, 0.2T (3.9s)

In Fig 3.3(c) a velocity spike at center can be seen. This spike occurs because the flow is in exhalation mode and so flow is coming in from the daughter branches which eventually meets

at the bifurcation and this flow impingement at the center of the parent tube gives rise to a spike in the velocity profile. The height of the spike depends on the peak Reynolds number. Velocity spike was quite distinct for maximum Reynolds number of 2207 while it was less distinct for peak Reynolds number of 1072 or 700 and is unique to the exhalation mode.

Time: 0.2T, Location: Station 10

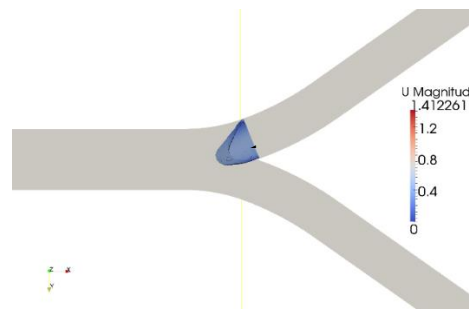
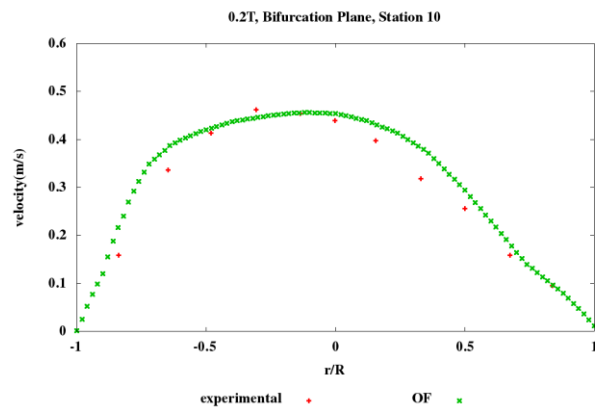


Fig 3.3(d): Case B Velocity Profile at Station 10, 0.2T (3.9s)

Another important feature captured by the simulation is the skewness of the velocity profile, (Fig. 3.3(d)) during exhalation, towards the inner wall of the bifurcation due to the curved geometry and associated secondary vortices.

Time: 0.2T, Location: Station 15

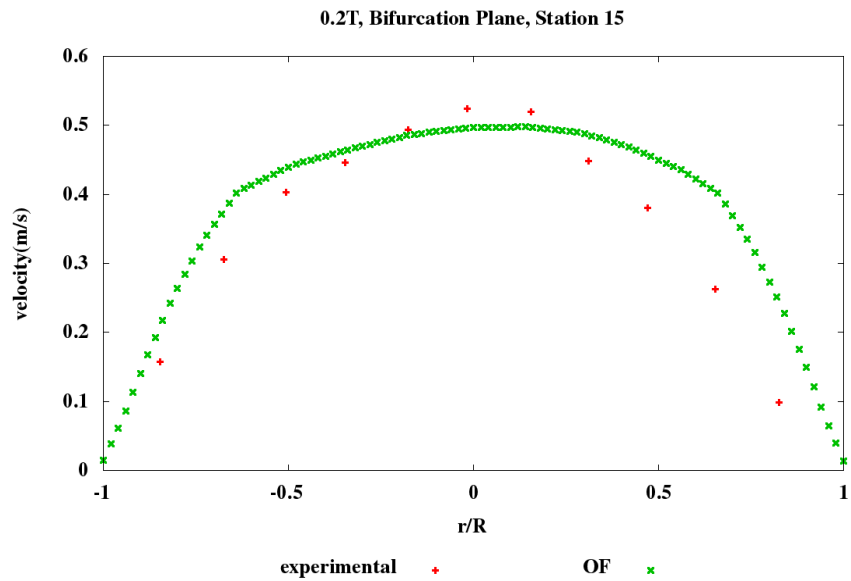


Fig 3.3(e): Case B Velocity Profile at Station 15, 0.2T (3.9s)

Time: 0.7T, Location: Station 2

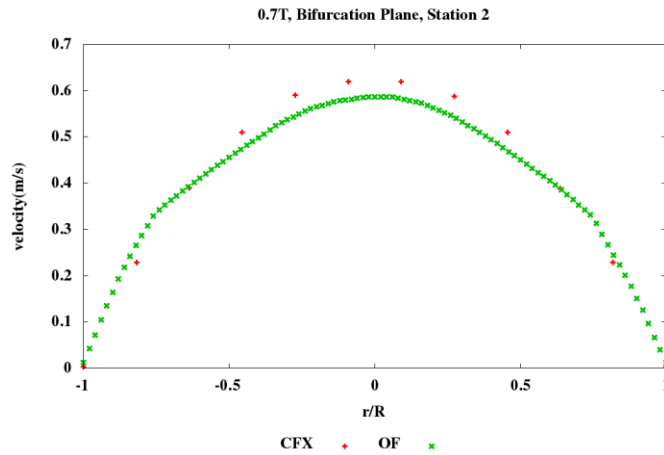


Fig 3.3(f): Case B Velocity Profile at Station 2, 0.7T (13.7s)

At 0.7T (13.7s) flow is at peak inspiration and as expected the velocity profile is fully developed, in the parent tube, as per the input waveform.

Time: 0.7T, Location: Station 10

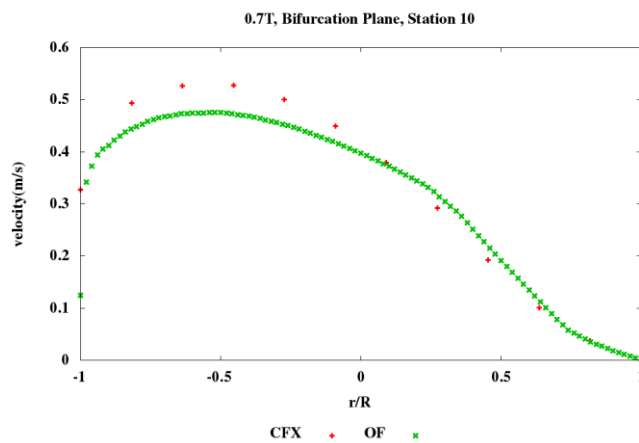


Fig 3.3(g): Case B Velocity Profile at Station 10, 0.7T (13.7s)

By observing the velocity-profiles of Fig. 3.3(c) to Fig. 3.3(f), we find that results from the OpenFOAM simulation model are in good agreement with experimental and CFX data sets. They are both accurate in time and space. This simulation captures main features, such as the velocity spike (Fig 3.3(c)) seen at 0.7T and Station 2, skewness in the bifurcations, fully developed profile in the straight section, etc.

3.4 Case C: Airflow Field with Particle Distribution

Bushi et al. (2005) performed an experiment in an asymmetric single bifurcation model with particles of sizes 0.6 mm, 1.6 mm and 3.2mm. It was found that small (0.6mm) and medium (1.6mm) sized neutrally buoyant particles entered in each branch non-preferentially, i.e., proportional to flow ratios. This experimental observation was reproduced by numerical simulations using OpenFOAM's Lagrangian particle tracking solver '*icoUncoupledKinematicParcelFoam*' and steady-state solver '*simpleFoam*'. It also provided a good platform to validate OpenFOAM's Lagrangian particle solver and drag model.

3.4.1 Geometry and Mesh

An in-house geometry already created for validations using CFX was employed. The geometrical features were adapted from Bushi et al (2005). In Fig. 3.4(a), $D_0=D_1=6\text{mm}$, $D_2=4\text{mm}$ and $\theta_1=\theta_2=45^\circ$. A mesh containing 0.6 million elements was created with ANSYS ICEM 14.0, using dense prism layer elements at the wall and tetrahedral elements at the core.

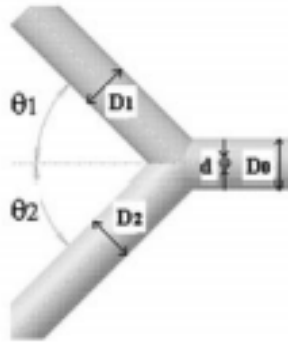


Fig 3.4(a): Case C Geometry Schematic

3.4.2 Governing Equations, Boundary Condition and Numerical Scheme

OpenFOAM's *simpleFoam* solver was used to solve Continuity equation (1) and Navier Stokes equation (2) for an incompressible, 3D, laminar flow under steady state conditions using the same numerical scheme as used in Validation A and transient Lagrangian particle tracking solver, *icoUncoupledKinematicParcelFoam*, was used to solve Newton's Second Law Equation (4).

First, a steady-state flow field was calculated at a prescribed Reynolds number of 500 at the inlet with a fully-developed velocity profile and a convergence criterion of 10^{-5} . No-slip boundary condition was invoked at the boundary surfaces of the geometry. A converged velocity field was then given as an initial condition for the Lagrangian particle-tracking solver. As particle distribution measurements were made at each outlet for four different outlet flow rates, i.e., 1:1, 2:1, 3:1, and 4:1, four sets of velocity fields were calculated by setting up four simulation cases and prescribing different flow rates at outlets in each case. Similarly, four different Lagrangian particle-tracking cases were set up, using the flow fields calculated in

each case.

Neutrally buoyant particles of two sizes, i.e., 0.6 cm and 1.6 cm, were used for this validation. Since the particle used were neutrally buoyant the effect of gravity was neglected, while drag force and pressure gradient force (see Eq.12, Eq.18 in Section 2.4) were taken into account. Uniform particle distribution was used at the inlet. Using the parabolic inlet particle distribution (Zhang & Kleinstreuer, 2001) gave the same results which were consistent with experimental observation.

3.4.3 Results and Discussion

In the Fig 3.4(a), $N1/N2$ represents the ratio of particles coming out of outlet 1(6mm) to outlet2 (4mm, see Fig 3.4a) while $Q1/Q2$ represents the ratio of volume flow rate distribution between outlet1 and outlet2. It is clear from the plot that our numerical results were in agreement with experimental observation and indeed particles are distributed in accordance with flow ratios.

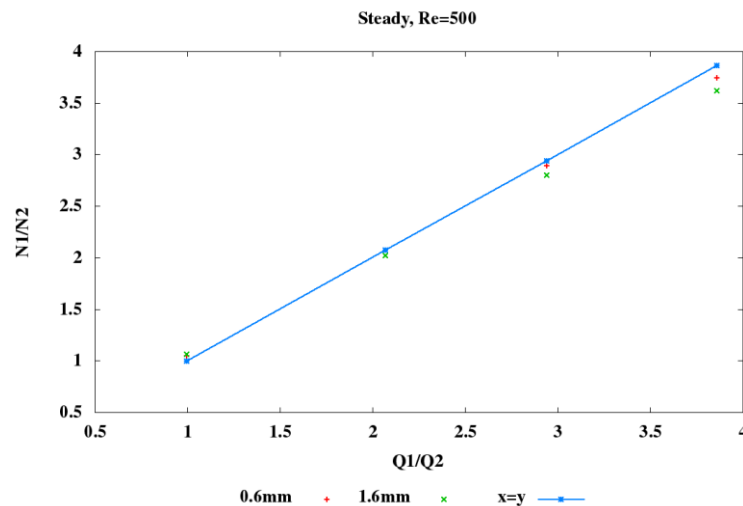


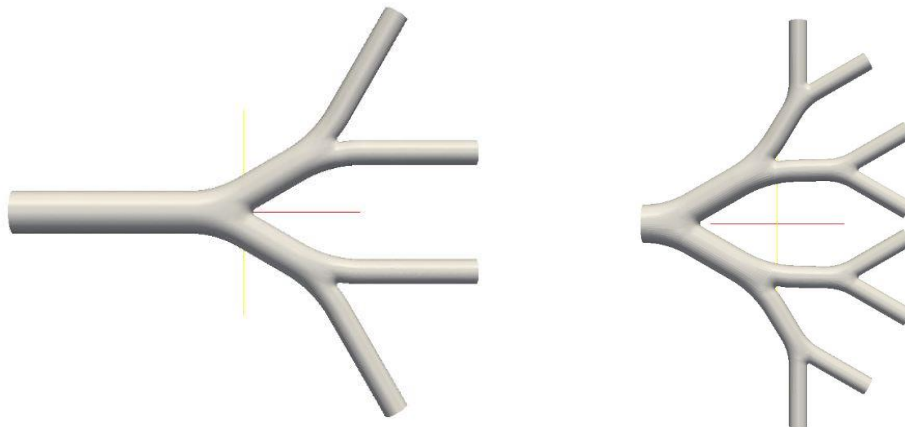
Fig 3.4(b): Case C Result

3.5 Case D: Particle Deposition in double and triple bifurcation

Simulated in this validation are the particle Deposition Efficiency (DE) in an idealized symmetric double bifurcation and triple bifurcation geometries adapted from Weibel (1963) lung model. Our numerical results show good agreement with Kim and Fisher (1999) experimental results and in house ANSYS CFX simulation results. Based on the confidence from a good match of double bifurcation results, DE's in triple bifurcation were simulated and compared with published numerical results of Zhang et al (2001). In summary a good agreement was seen between OpenFOAM, ANSYS CFX and available experimental results.

3.5.1 Geometry and Mesh

Both the triple and double bifurcation geometries were available in-house.



(a) Double bifurcation (Kim and Fisher, 1999) (b) Triple Bifurcation (Zhang et al,2001)

Fig 3.5: Case D Representative Geometries

An in-house hexahedral mesh (0.6 million cells) was used to simulate DE's in triple bifurcation geometry while tetrahedral and prism elements mesh (1.8 million cells) was

created for double bifurcation geometry using ANSYS ICEM 14.0. Mesh sizes were determined by performing mesh independence tests on both triple and double bifurcation geometries.

3.5.2 Governing Equations, Boundary Condition and Numerical Scheme

OpenFOAM's *simpleFoam* solver was used to solve Continuity equation (1) and Navier Stokes equation (2) for an incompressible, 3D, laminar flow under steady state conditions using the same numerical scheme as used in validation Case A and transient Lagrangian particle tracking solver, *icoUncoupledKinematicParcelFoam*, was used to solve Newton's Second Law (Eq. 4, Section 2.2)

For steady-state flow field calculations a fully-developed inlet velocity profile was specified with an inlet Reynolds Number of 1200 for double bifurcation geometry and Reynolds Number of 800 for triple bifurcation geometry. Uniform fixed pressure boundary condition was defined at each outlet. Since the pressure was fixed at the same value equal flow rate distribution was seen at all the outlets. No slip velocity boundary condition was invoked at the boundary surfaces.

Particles were assumed to stick to the wall once when they are one radius away from the wall and were assumed to escape once they reach the outlet. Since the assumed particle density is large as compared to that of fluid (air) only drag and gravitational forces were assumed rest of the forces were discounted (Zhang and Kleinstreuer, 2001).

3.5.3 Results & Discussion

Results in this section are presented as a function of particle inlet stokes number which is defined as:

$$St = \frac{\rho_p d_p^2 U}{18\mu D_1} \dots\dots\dots(26)$$

Where ρ_p is particle density, d_p is particle diameter, U is average inlet velocity, μ is fluid dynamic viscosity and D_1 parent (inlet tube) tube diameter. The Stokes number on x-axis are on logarithmic scale. DE on the y-axis in percentage (%) form.

Double Bifurcation Results: First Bifurcation

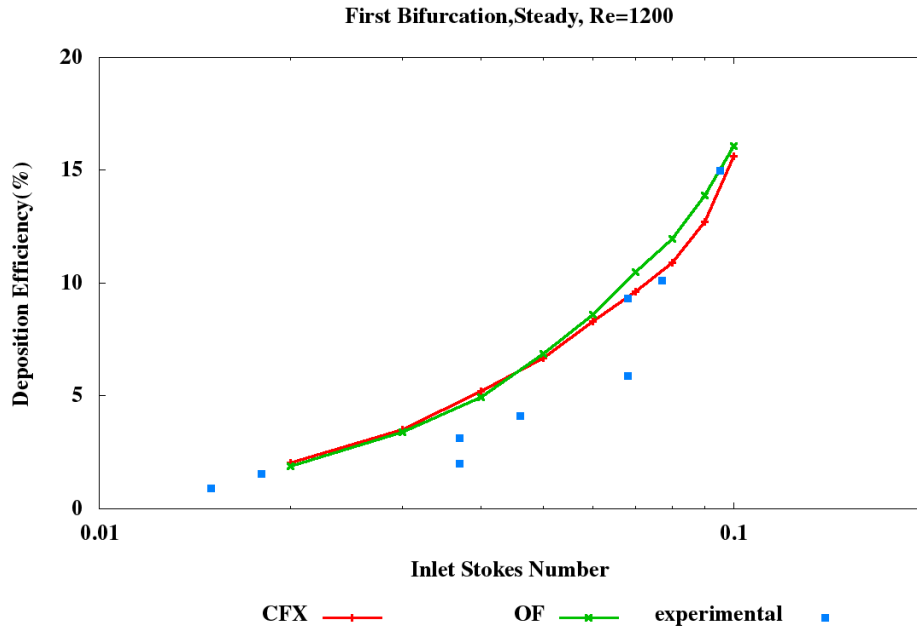


Fig 3.5 (c): Case D Particle Deposition in First Bifurcation

Double Bifurcation Results: Second Bifurcation

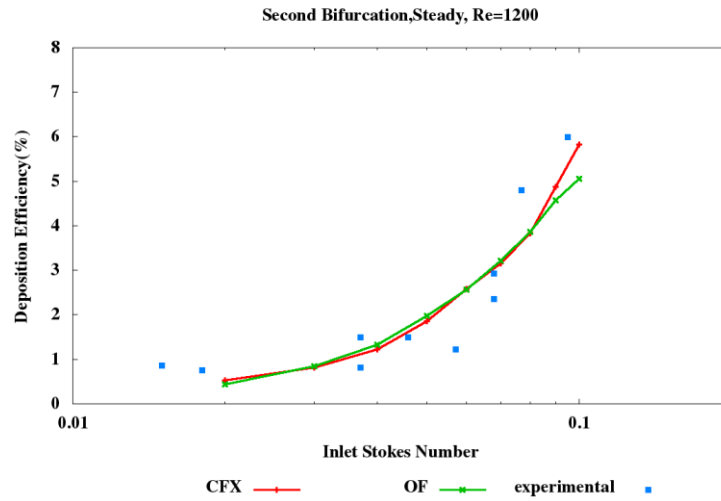


Fig 3.5 (d): Case D Particle Deposition in Second Bifurcation

Triple Bifurcation Results: First Bifurcation

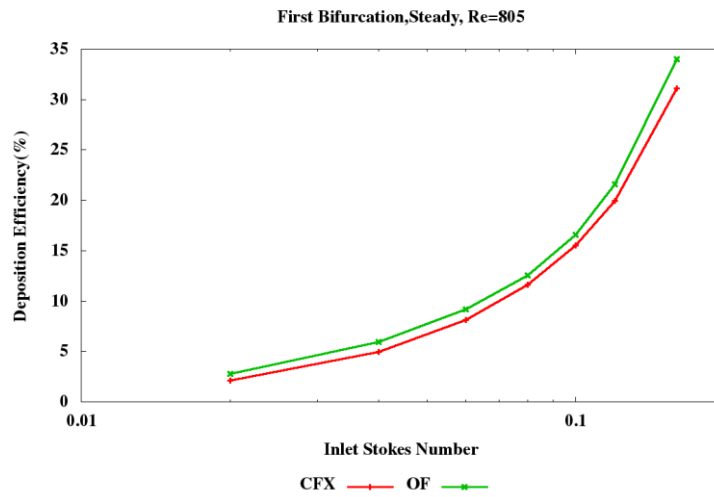


Fig 3.5 (e): Case D Particle Deposition in First Bifurcation

Triple Bifurcation Results: Second Bifurcation

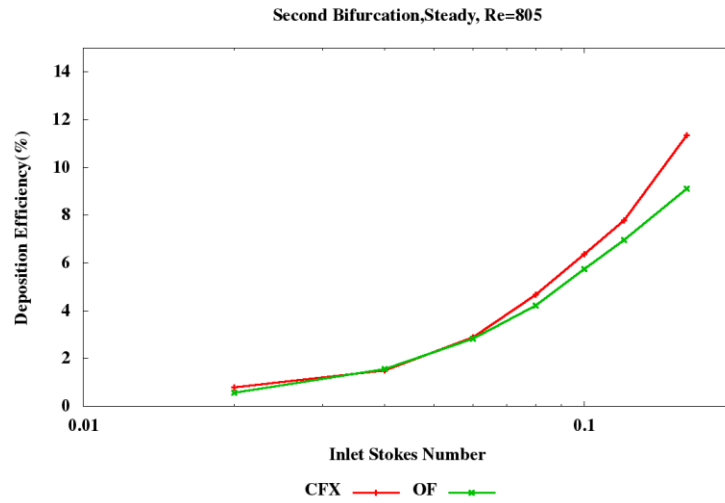


Fig 3.5 (f): Case D Particle Deposition in Second Bifurcation

Triple Bifurcation Results: Third Bifurcation

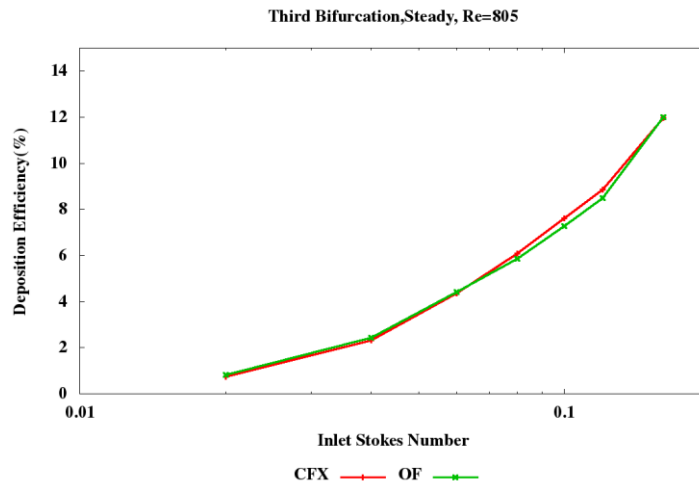


Fig 3.5 (g): Case D Particle Deposition in Third Bifurcation

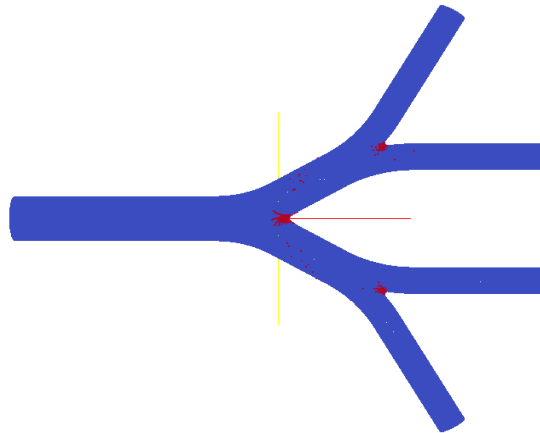


Fig 3.5 (h): Case D Particle Deposition Pattern in Third Bifurcation

From Fig 3.5 (f) it is evident that most particles (red portion) deposit around cranial ridges since inertial impaction is mainly responsible for particle deposition in microspheres and for the same reason there is hardly any deposition in straight section (trachea) of the tube.

Our results (3.5(c)-3.5(g)) show that the OpenFOAM simulation results reasonably trace the DE patterns of microspheres when compared with experimental and CFX results. Variations may be due to difficulty in strictly controlling the flow rate and aerosol diameters, so Reynolds Number may vary considerably in experiments. Furthermore, some variations between computational predictions and experimental results may be due to subtle differences in model geometries and deposition measurements.

3.6 Software Performance Analysis: CFX vs. OpenFOAM

A comparison study was done between commercial CFD code CFX 14.0 and open-source CFD code OpenFOAM. The objectives were to compare speed of computation, ease-of-use

and accuracy. For example, a simple flow simulation, i.e., steady laminar incompressible, was done with the same geometry, boundary conditions and numerical schemes as in validation Case A. The first mesh contained 0.6 million cells (coarse mesh) while the other contained 1.2 million cells (fine mesh) to take into account the behavior of different codes w.r.t. mesh sizes. The same convergence criterion (10^{-4}) was used in all the cases, where the simulations were executed with a single processor on the same machine.

3.6.1 Results: Coarse Mesh

Please refer to Fig 3.2(a) for geometry and probe locations.

The coarse mesh contained 0.6 million cells with tetrahedral and prism layers. CFX took 434.4 seconds while OpenFOAM took 25462.8 seconds to give a converged solution. Thus, CFX was

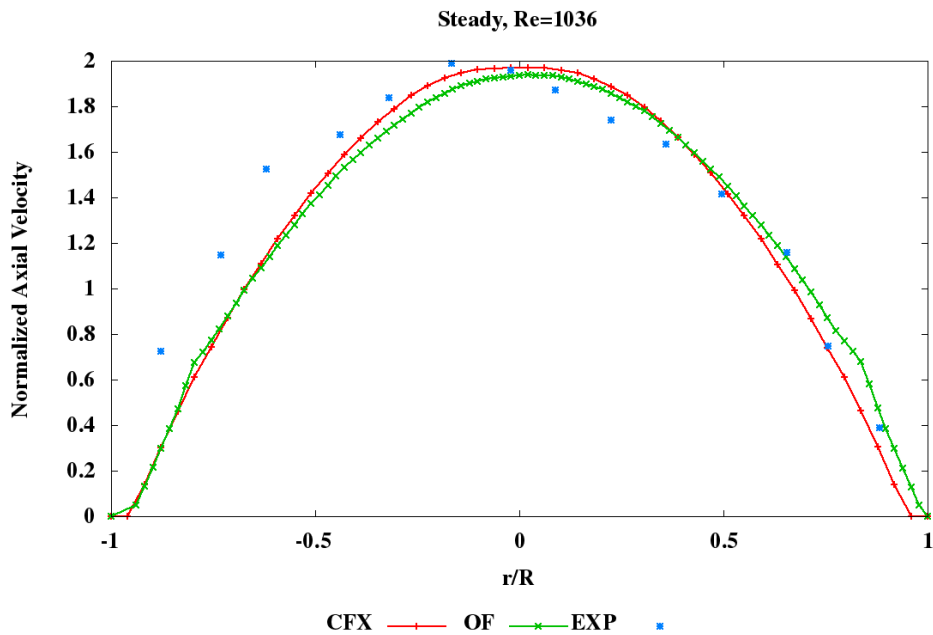


Fig 3.6 (a): Coarse Mesh Comparison at A-A'

58 times faster than OpenFOAM in this case. As far as the accuracy is concerned, there were no major differences (see Fig 3.6(a) and Fig 3.6(b)).

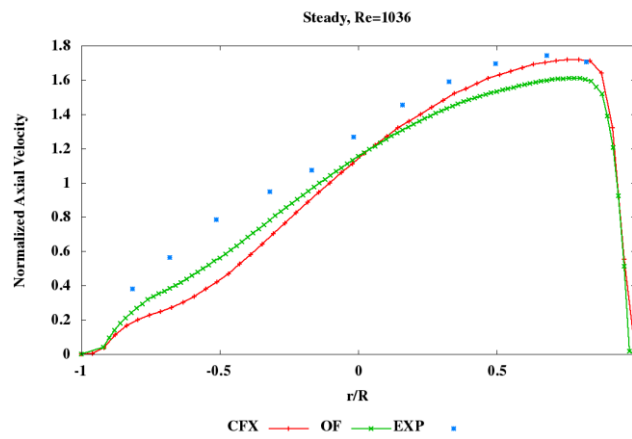


Fig 3.6 (b): Coarse Mesh Comparison at B-B'

3.6.2 Results: Fine Mesh

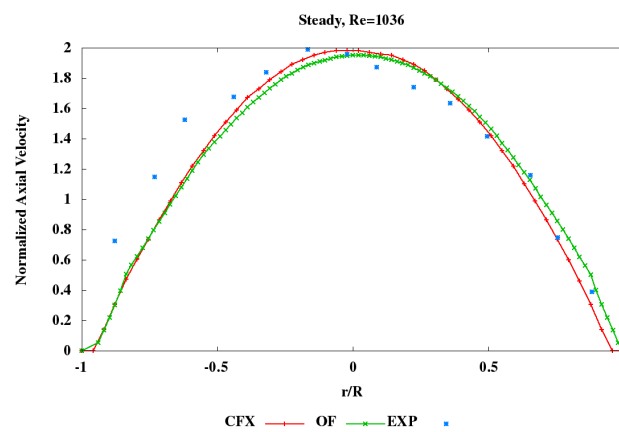


Fig 3.6 (c): Fine Mesh Comparison at A-A'

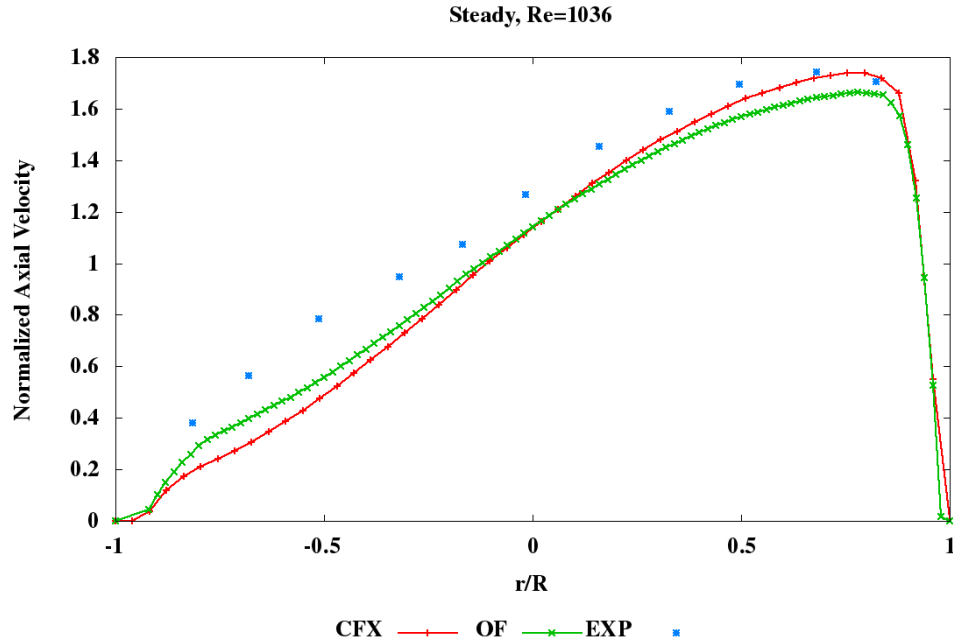


Fig 3.6 (d): Fine Mesh Comparison at B-B'

The fine mesh contained 1.2 million cells with tetrahedral and prism layers. CFX took 662.2 seconds while OpenFOAM took 140800 seconds to give a converged solution. Thus CFX was 212 times faster when compared to OpenFOAM in this case. As far as the accuracy is concerned, there were no major differences.

The large difference in computational speed can be attributed to numerical approach adopted for obtaining the solution of Navier-Stokes Equation (see Eqs. (1 and 2) in Section 2.1). The major difference between OpenFOAM and ANSYS CFX lies in their basic discretization approach. OpenFOAM achieves the spatial discretization by using the finite volume method (FVM) on block structured meshes with Gaussian integration and linear interpolation. From

the available techniques, temporal discretization is obtained with equidistant implicit Euler blended Crank-Nicolson time stepping scheme (blending factor = 0.5). Later, pressure and momentum equations are decoupled by using the PISO algorithm (Ferziger and Peric, 2002). For the solution of the momentum equation, PBiCG is employed. The pressure equation is solved by using a Geometric-Algebraic Multigrid solver with a Gauss-Seidel type smoother. ANSYS CFX employs an element based finite volume approach to discretize in space and a high resolution scheme is chosen for the stabilization of the convective term. Time discretization is achieved by Second Order Backward Euler scheme. Tri-linear finite element based functions are used as interpolation scheme. ANSYS CFX uses a coupled solver, which solves the hydrodynamic equations (for u , v , w , p) as a single system. First, nonlinear equations are linearized (coefficient iteration), then these linear equations are solved by an Algebraic Multigrid (AMG) solver.

Thus, in conclusion better numerical discretization schemes and fully implicit coupled solvers, which are more robust and stable way of obtaining solution, can be programmed and integrated with OpenFOAM source code to improve its speed of computation.

CHAPTER 4

OpenFOAM SOFTWARE APPLICATIONS

4.1 Turbulence Model Validation

As discussed in section 2.1 at moderate to high breathing rates, i.e., $Q_{in} > 12$ L/min, the airflow from the larynx to generation G3 is transitional-to-turbulent which may complicate flow structures as well as aerosol transport and deposition (Kleinstreuer and Zhang, 2003a and Zhang and Kleinstreuer, 2004). OpenFOAM's *kkLOmega* was selected to predict and capture transitional behavior of fluid flow in idealized and realistic oral airway models. In the following sections, I have presented a comparison between predictions based on *kkLOmega* turbulence model (OpenFOAM), LRN $k - \omega$ turbulence model(CFX) and experimental data (Ahmed and Giddens, 1983).

4.1.1 Stenosed Tube Geometry and Mesh

For this validation study a conduit with smooth sinusoidal constriction, causing 75% area reduction (Fig 4.1(a)), was selected and the fluid-flow results were compared for $Re_{in}=500$ and 2000 with experimental data of Ahmed and Giddens(1983) as well as CFX results. At the inlet uniform velocity profiles were specified. A high quality mesh of 0.86 million cells consisting of purely hexahedral elements was generated, using ANSYS ICEM 14.0 with structured O-grid. An axisymmetric conduit with minimum cross sectional area at the middle was constructed on SOLIDWORKS. The diameter of the conduit from $z=0$ to $z=D$ was varied sinusoidal (see Eq. (27)).

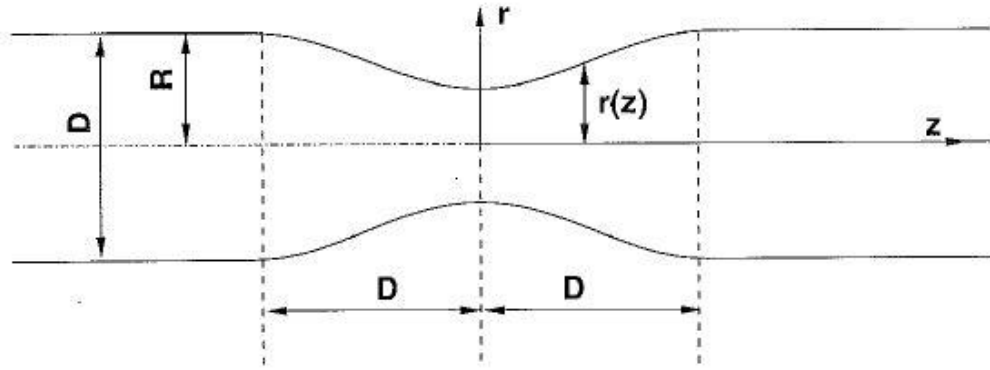


Fig 4.1(a): Turbulence Model Validation Geometry Schematic

$$r(z) = \left\{ \begin{array}{ll} R - \frac{R}{2} \cos\left(\frac{\pi z}{2D}\right) & \text{if } |z| \leq D \\ R & \text{if } |z| > D \end{array} \right\} \dots\dots\dots (27)$$

4.1.2 Governing Equations, Boundary Conditions and Numerical Schemes

OpenFOAM's *simpleFoam* solver was used to solve Continuity Equation(1), Navier Stokes Equation(2) and additional transport equations to calculate eddy viscosity via Eq.37-39 (see Appendix A) for an incompressible, 3D, transitional flow under steady state conditions.

Constant velocity profile with Reynolds Number of 500 and 2000 was specified at the inlet. Higher order schemes (Self Filtered Central Differencing Scheme) scheme and Gauss linear corrected schemes were used to model convective and diffusive terms respectively.

At the outlet '*zeroGradient*' boundary condition was specified for velocity while a reference fixed value was specified for pressure. For turbulence parameter k_T (turbulent kinetic energy),

k_L (laminar kinetic energy) and ω (scale – determining variable) following were boundary

conditions were used:

At solid boundaries, the no-slip condition enforces

$$k_T = k_L = 0 \dots\dots\dots (28)$$

A zero-normal-gradient condition is used for ω :

$$\frac{\partial \omega}{\partial \eta} = 0 \dots\dots\dots (29)$$

Where η is the wall-normal coordinate direction.

At flow inlets, the value of k_T and ω are prescribed exactly analogous to LRN $k - \omega$ model equations (Wilcox, 1998). The turbulent kinetic energy (k_T) is often determined based on the inlet turbulence intensity (I):

$$k_T = 1.5(I \times u_{in})^2 \dots\dots (30)$$

$$\omega = k_T / 0.3D \dots\dots (31)$$

$$k_L = 0 \dots\dots\dots (32)$$

Where I , u_{in} , D are turbulent intensity (assumed to be 0.37), inlet average velocity and inlet diameter, respectively.

At flow outlets, all the turbulence model parameters were kept at ‘zeroGradient’ boundary condition.

4.1.3 Results and Discussion

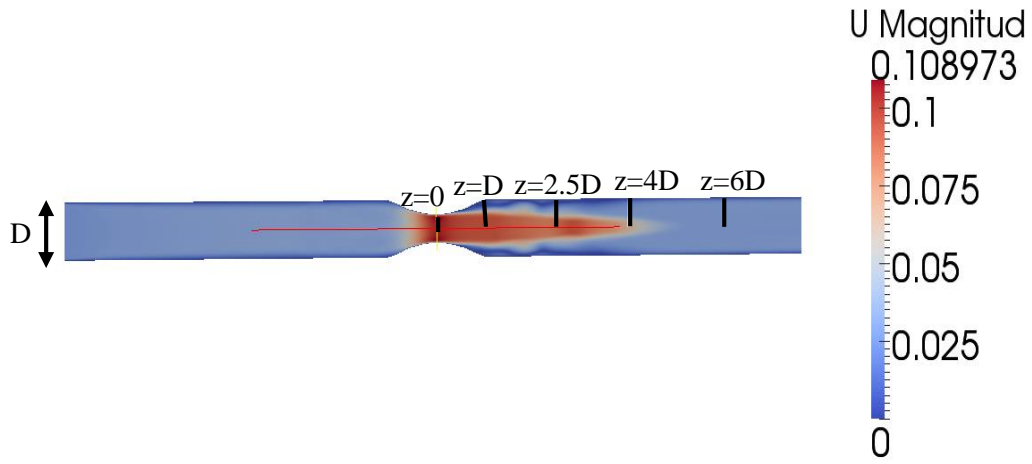


Fig 4.1(b): Turbulence Model Validation Result Probe locations

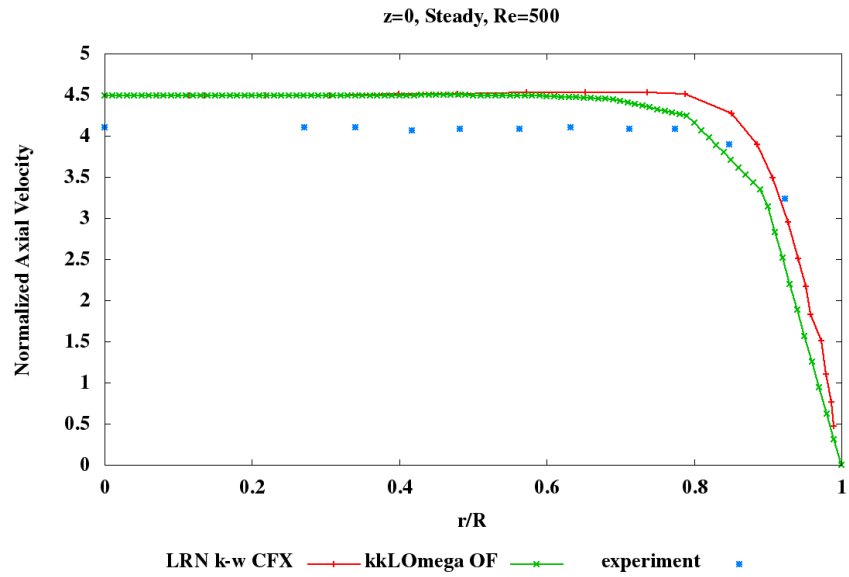


Fig 4.1(c): Turbulence Model Validation Result at $z=0$, $Re=500$

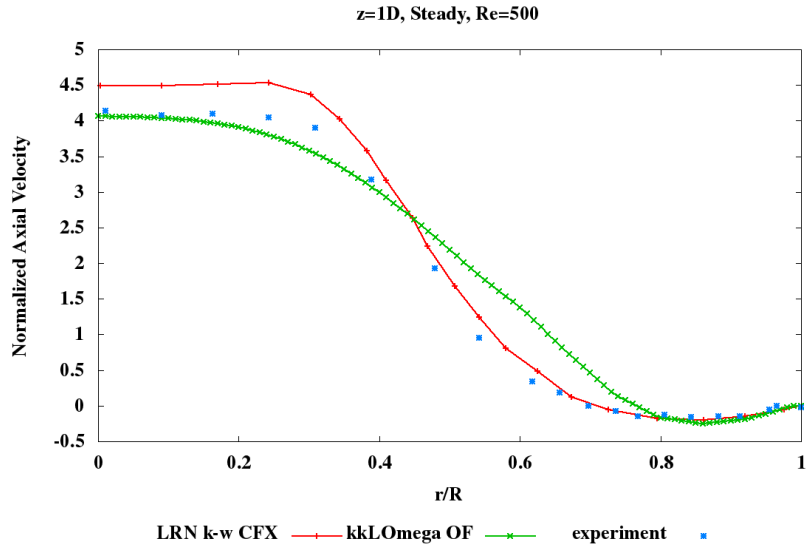


Fig 4.1(d): Turbulence Model Validation Result at z=D, Re=500

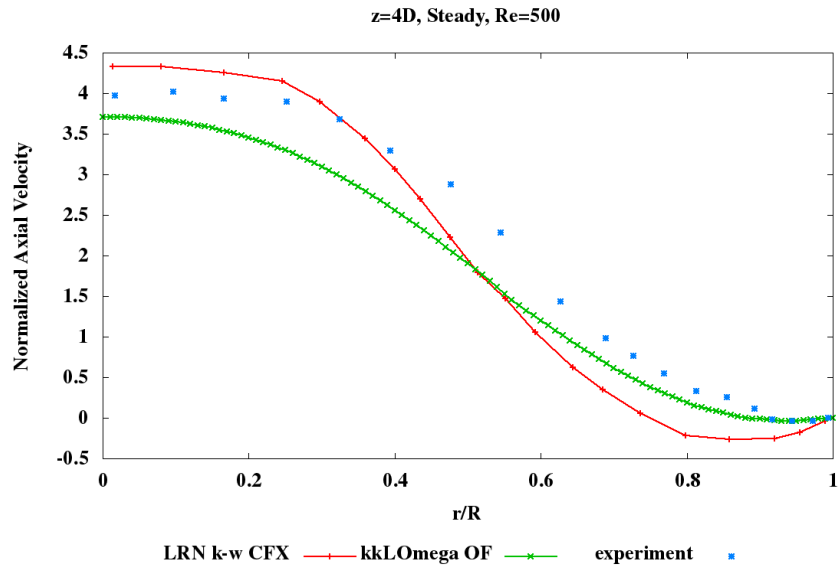


Fig 4.1(e): Turbulence Model Validation Result at z=4D, Re=500

Fig 4.1(b) indicates a uniform inlet velocity profile, due the effect of turbulence and change in the shape of the cross-section this profile undergoes changes further downstream. The experimental study indicated that the flow fluctuations tend to be very weak in case of $Re_{in}=500$, and no post-stenotic turbulence was observed. This is very much apparent from the Fig 4.1(c)- Fig 4.1(e) since full transition to turbulence which is indicated by a blunt velocity profile (Fig 4.1(i)) cannot be seen for $Re_{in}=500$.

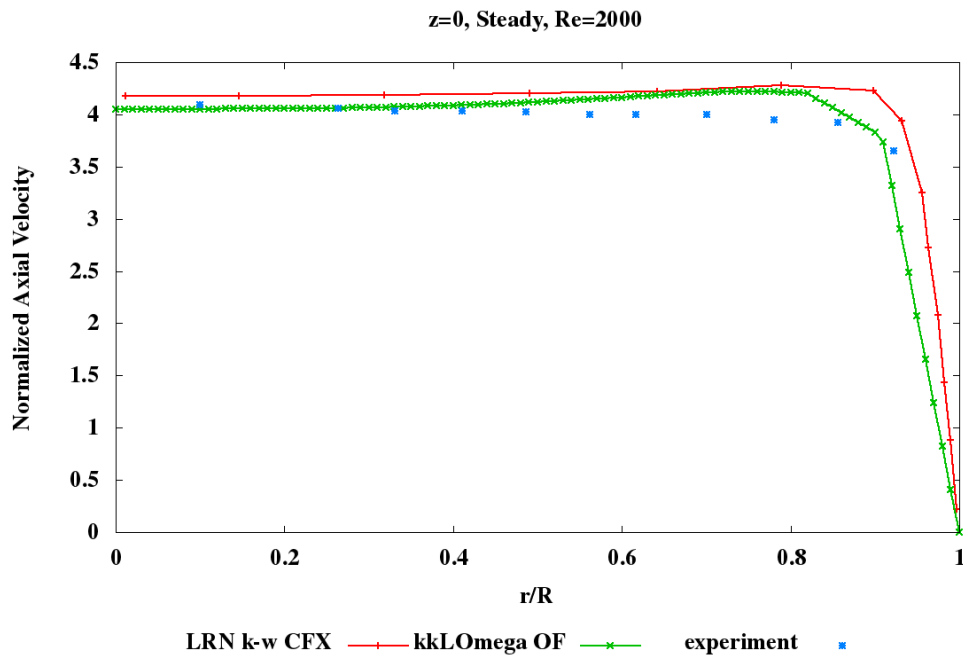


Fig 4.1(f): Turbulence Model Validation Result at $z=0$, $Re=2000$

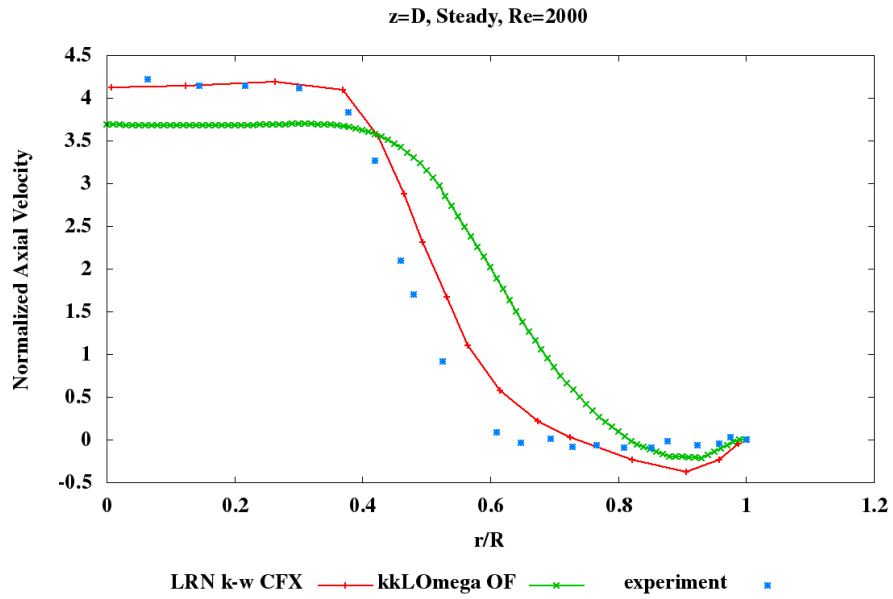


Fig 4.1(g): Turbulence Model Validation Result at z=D, Re=2000

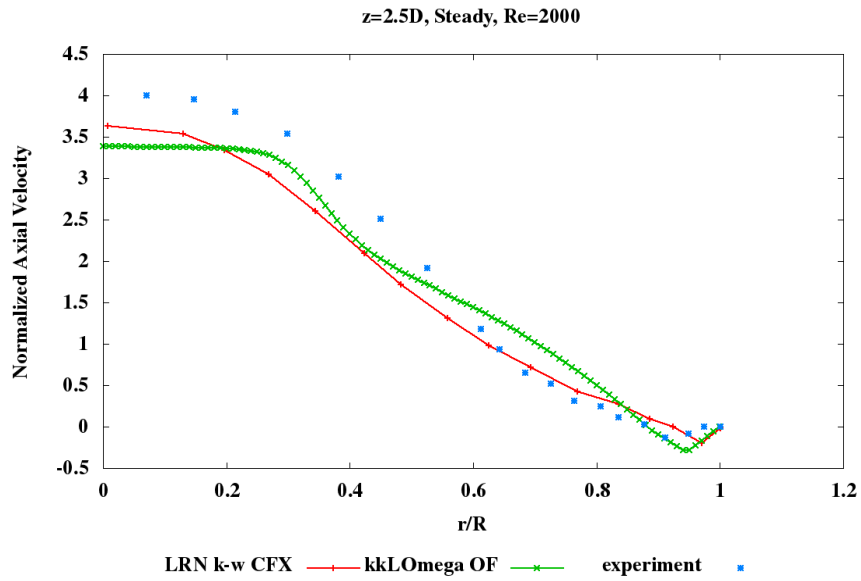


Fig 4.1(h): Turbulence Model Validation Result at z=2.5D, Re=2000

It was seen the that there was slow decrease in the magnitude of centerline velocity until $z=2.5D$ but there was rapid decrease in the centerline velocity after it due to area expansion and transition to turbulent flow in conjunction with large scale momentum transfer. It can also be seen that velocity profile became fully blunt (Fig 4.1(i)) around $z=6D$ indicating full transition from laminar to turbulent flow.

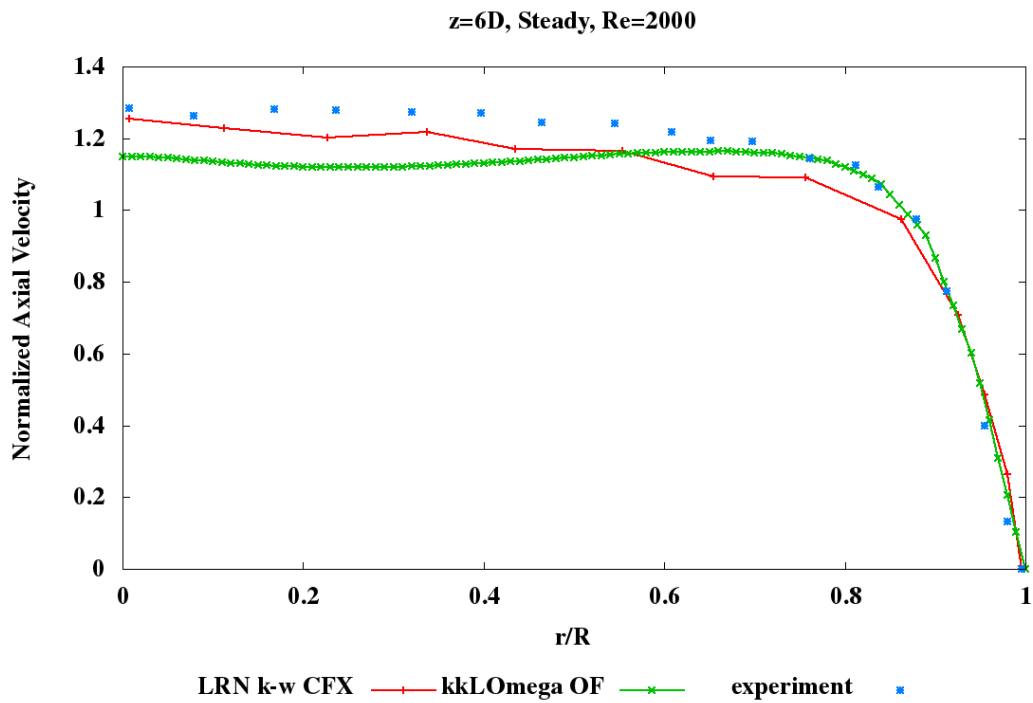


Fig 4.1(i): Turbulence Model Validation Result at $z=6D$, $Re=2000$

The simulation of flow in a rigid tube with an axisymmetric constriction (Fig 4.1(a)) was performed to assess the *kkLOmega* turbulence model. Ahmed and Giddens (1983) conducted experimental measurements focusing on the velocity fields in the neighborhood of the same axisymmetric constriction at inlet Reynold's Number of 500 to 2000. From Fig 4.1(c)-Fig 4.1(i) we can see that results based on *kkLOmega* (OF), LRN $k-\omega$ (CFX) and experimental results are in good agreement. Clearly, the *kkLOmega* model captures very well the flow characteristics after the stenosis, including 1) the nearly uniform flow at the throat, 2) the development of the shear layer and the recirculatory flow before $z=4D$ and 3.) the occurrence of transition to turbulence indicated by rather blunt velocity profile after $z=5D$ caused by the redistribution of the kinetic energy of the flow over most of the cross section. Some differences can be observed at stations $z=2.5D$, $4D$ and $5D$. This can be attributed to the increasing experimental uncertainty in regions where the velocity profile change rapidly as a result of the local onset of turbulence.

4.2 Trumpet Model

A trumpet model reduces the complex human respiratory tract to a simple 1-D configuration with expanding cross-sectional area, which resembles geometrically a trumpet. Thus, it is easy to execute, requires little computational resources, and is quite useful if it can accurately predict overall particle depositions. For example, considering global micron-particle deposition in a subject-specific lung model *vs.* the present trumpet model, a typical computer run-time ratio is 200 as per the simulations performed in-house using CFX. Until now particle depositions calculated with the trumpet model (see Fig 4.3(a)) was done by employing a modified form of

the convection-diffusion equation (Taulbee et al. 1975, Darquenne et al. 1994, Kim et al. 2007). The common approach was that researchers incorporated loss terms, i.e., loss of particles to the airway wall by inertial impaction, sedimentation, and diffusion. They used mathematical correlations based on experiments (Schlesinger et al. 1972) or derived theoretically (Beeckmans et al. 1965). Calculation of particle deposition by employing Newton's Second Law has not been investigated. So, initial simulations using the Euler-Lagrange approach with an in-house constructed trumpet geometry were carried out, considering only the drag force and gravity for micron particles. As expected, the deposition fractions calculated using this approach were way too low than those found experimentally or calculated by performing simulations on realistic geometries. The reason for this discrepancy is that for micron particles deposition takes place mainly due to inertial impaction; however, the trumpet model closely resembles a diverging straight tube so that particles exit without any obstructions, such as carinal ridges.

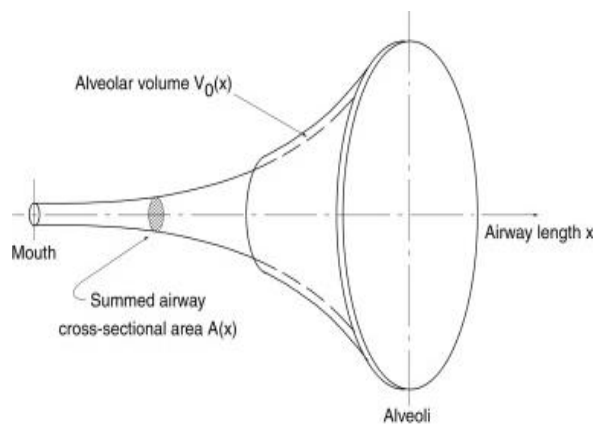


Fig 4.2(a): One dimensional trumpet model (Hofmann, 2011)

4.2.1 Novel Approach and Methodology

In this approach, calculating the particle deposition is based on a ‘modified’ Lagrangian model, i.e., a new radial force function has been developed which along with the regular drag force generates actual particle trajectories towards the wall. Hence, the overall particle deposition fractions are in agreement with experimental data sets. The new semi-empirical force is a function of the average inlet velocity corresponding to specific inlet volumetric flow rates (e.g., 15L/min, 30 L/min, etc.), particle diameter, breathing rate, and lung volume. The force will point in radial direction at each cross-section so that particles move towards the wall for deposition.

For one test case an average inspiratory flow rate of 15L/min, a tidal volume (volume of air intake in one breath) of 500ml and lung volume of 3000ml was considered. First the forces were found to give the required experimental particle deposition and the data was curve-fitted in a simple linear fashion in terms of particle diameter to obtain a correlation specific to the listed parameters. After that the obtained correlation were multiplied by appropriate ratios to produce the particle-deposition shift (see Kim et al., 2007) according to the changes in parameters such as average inspiratory flow rate, tidal volume or total lung volume. Equation (33) in Section 4.2.4 provides some details.

4.2.2 Geometry and Mesh

As mentioned, the human airway system was approximated by a one-dimensional, variable cross-section channel, where the cross-sections are functions of the generation number of a given symmetric lung model, typically the Weibel Model A (Taulbee & Yu, 1975). Thus each

airway branch within a given generation has identical dimensions and is characterized by its axial distance from the origin of the trachea. In the acinar generations, additional volume for the alveoli encircles the channel. The cross-sectional area increases sharply with distance from the trachea adopting a trumpet-like shape, hence the name ‘trumpet’ model (Fig. 4.3(a)).

A geometry was constructed based on data obtained from the Weibel Model A. A high quality mesh was created on ANSYS ICEM 14.0 with dense prism layer and tetrahedral core.

4.2.3 Governing Equations, Boundary Conditions and Numerical Schemes

Volume flow rate boundary condition was prescribed at the inlet while the outlets were kept at uniform fixed pressure condition. No slip boundary condition was invoked at solid boundary surfaces.

Uniform particle density was specified at the inlet. Particle with aerodynamic diameter ($2 \mu\text{m}$ - $10 \mu\text{m}$) and two flow rates were considered in developing correlation, i.e., 15L/min and 30L/min. *simpleFoam* solver, numerical schemes and solution controls as stated in Sec.4.1.2 were used.

4.2.4 Results and Discussions

Correlation:

$$\overline{F_rad} = vratio^{(-0.2)}.qratio^{(0.5)}.ratio^{(1.35)}.((4.821e-06).d - (7.566e-12)).\vec{i} \dots\dots\dots (33)$$

- $\overline{F_rad}$ = radial force vector
- *vratio* = ratio of total lung volume to be simulated to 3000ml. Multiplying by this ratio, raised to the exponent (-0.2), adjusts the particle deposition curve to fit the experimental deposition data in case the simulated lung volume is not 3000ml.

- q_{ratio} = ratio of tidal volume to be simulated to 500ml. Multiplying by this ratio, raised to the exponent (0.5), adjusts particle deposition curve to fit the experimental deposition data in case the simulated tidal volume is not 500ml.
- $ratio$ = ratio of average inspiratory flow rate to be simulated to 15L/min. Multiplying by this ratio, raised to the exponent(1.35), adjusts the particle deposition curve to fit the experimental deposition data in case the average inspiratory flow rate is not 15L/min.
- d = particle diameter.
- \vec{i} = unit vector in radial direction

The experimental data were obtained from the results published by Hyder et al. (1986), Kim and Hu.,(1998) and Kim and Jacques (2000) for a Functional Residual Volume (FRC) of 3000ml. The particle deposition results are reported in terms of total deposition fraction which is the ratio of particle deposited in the entire lung to the number of particles entering the mouth inlet.

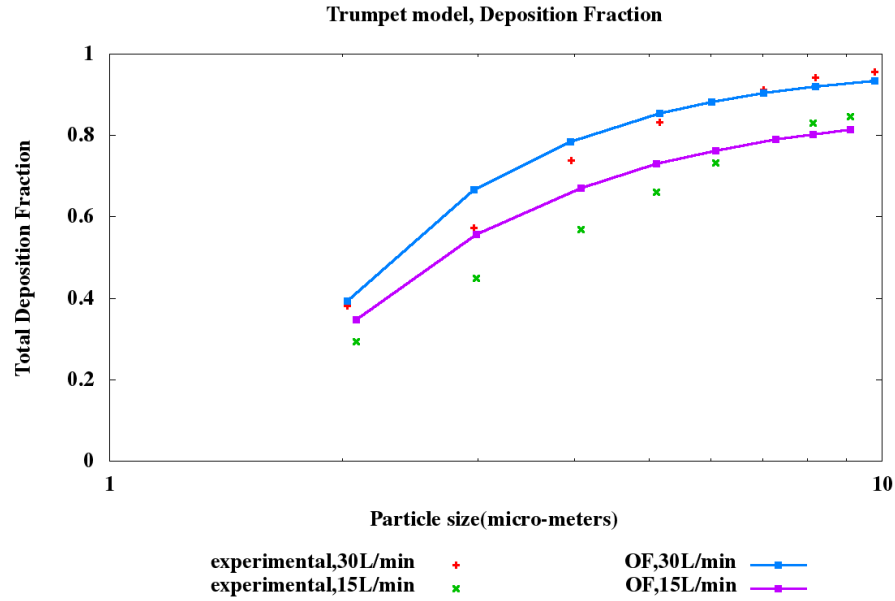


Fig 4.2(b): Particle Deposition Fraction at 30L/min, 15 L/min

Fig 4.2(b) compares the simulated total deposition fraction, obtained using the $\overline{F_{rad}}$ correlation (equation 33), with the experimental data. The correlation was found to give good results for particles with aerodynamic diameter from $2 \mu\text{m}$ - $10 \mu\text{m}$, which is useful as most toxic or therapeutic particles lie in this range. In this case following ratios were used:

- $v_{ratio}=1$; which implies lung volume is 3000mL
- $q_{ratio}=1$; which implies tidal volume is 500mL
- $ratio=1$; which implies inlet air flow rate is 15L/min
- $ratio=2$; which implies inlet air flow rate is 30L/min

From Fig 4.2(b) it follows that the particle deposition, for the same particle diameter, increases

as the average inlet flow increases. This is because higher initial air flow rate implies higher initial particle velocity so number of particle striking the wall will increase. Hence, deposition increases due to inertial impaction in case of high inlet flow rate.

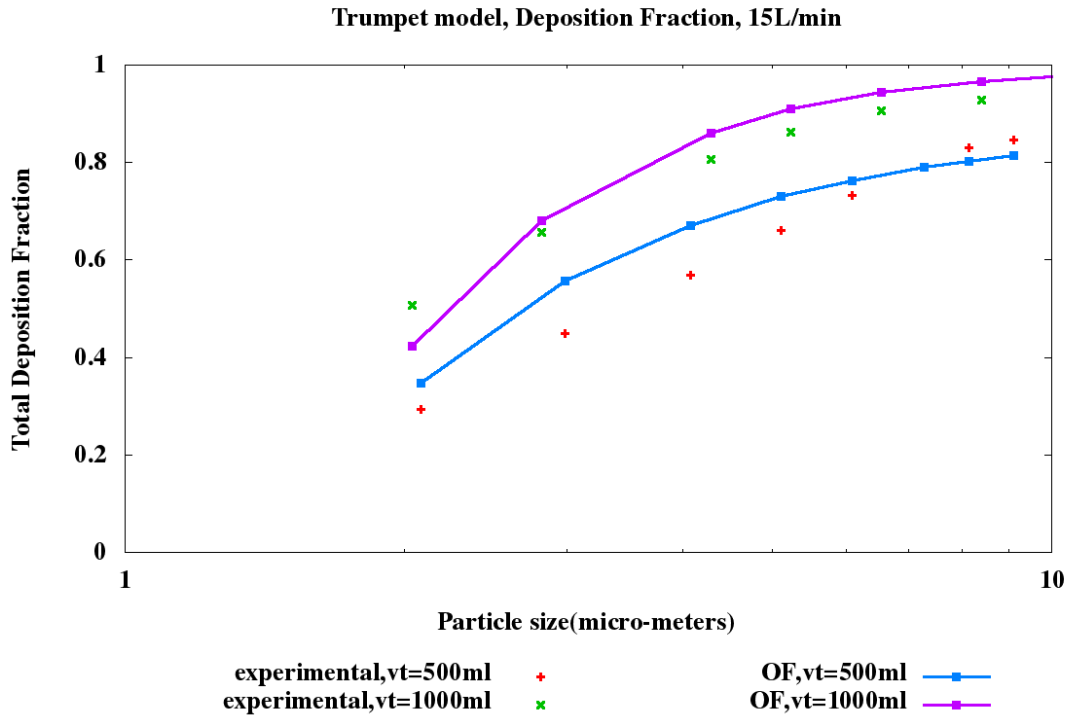


Fig 4.2(c): Particle Deposition Fraction at 15 L/min and tidal volume of 500ml, 1000ml

Fig 4.2(c) confirms that particle deposition results obtained by implementing $\overline{F_{rad}}$ correlation adjusts or provides required shift to fit the experimental data in case tidal volume is varied. Tidal volume basically defines the intake volume in one breath. Tidal volume

together with number of breaths per second or average inlet flow rate defines the breathing pattern.

Following values of ratios were used to generate particle deposition results:

- $v_{ratio} = 1$; which implies lung volume is 3000mL
- $q_{ratio} = 1$; which implies tidal volume is 500mL
 $q_{ratio} = 2$; which implies inlet air flow rate is 1000mL
- $r_{ratio} = 1$; which implies inlet air flow rate is 15L/min

As expected particle deposition, for same particle diameter, increases as the air flow rate per breath increases again due to increase in inertial impaction due to high initial particle velocity per breath.

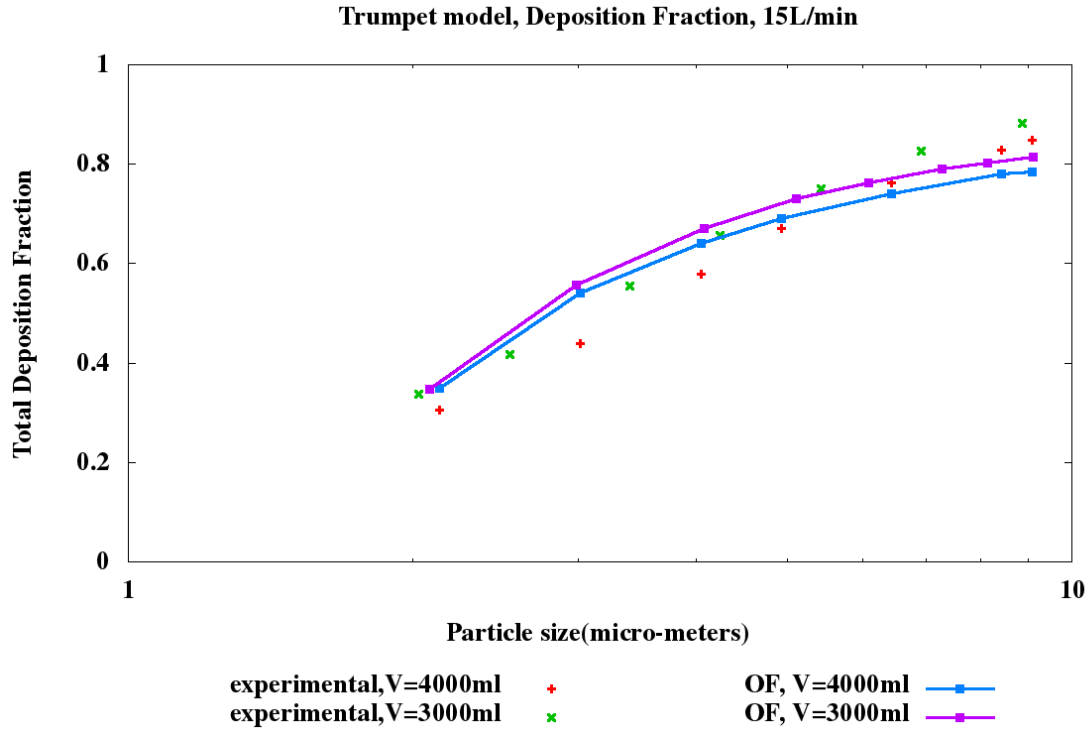


Fig 4.2(d): Particle Deposition Fraction at 15 L/min and total lung volume of 4000ml, 3000ml

Fig 4.2(d) shows the particle deposition curved obtained through simulation fits the experimental data. Following values of ratios were used:

- $v_{ratio}= 1$; which implies lung volume is 3000mL
- $q_{ratio}=1$; which implies tidal volume is 500mL
- $ratio=1$; which implies inlet air flow rate is 15L/min
- $ratio= 2$; which implies inlet air flow rate is 30L/min

Particle deposition, for same particle diameter, decreases as the air lung volume increases. This is because the airway dimension increases and particles have to travel little longer to reach the wall. The difference between total deposition fraction between 3000mL and 4000mL is less than 10% regardless of particle size and these results are consistent with recent experimental data showing virtually no total lung volume effects on microsphere deposition (Kim & Hu, 2006) in normal subjects.

CHAPTER 5

COMPARISON OF PARTICLE DEPOSITION SIMULATION RESULTS WITH *IN VIVO* EXPERIMENTAL STUDIES

5.1 Microsphere Deposition in Patient Specific Airway Geometry

The ultimate aim of the present lung-aerosol dynamics project is to simulate particle transport and deposition in patient-specific airways. Thus, after having provided a series of validations, in this chapter a simulation case is set up to simulate particle deposition in patient-specific airways. Specifically, microsphere deposition simulation results are presented, based on steady inhalation rates, i.e., 15L/min (light activity), 30 L/min (medium activity), and 60L/min (heavy activity). The OpenFOAM's *kkLOmega* turbulence model has been used (validated in Sect. 4.1) to calculate transitional laminar-to-turbulent flow in the present model. It has been established that the laryngeal jet occurring in the throat region induces turbulence immediately downstream, at inlet flow rates above 12L/min (Zhang et al., 2005). A comparison has been made between our OpenFOAM steady-state simulation results, CFX results, and available experimental data (Cheng et al., 1999).

5.1.1 Geometry and Mesh

A stereo-lithography (STL) file of the human airway model (Fig 5.1(a)) was generated using NextEngine's Desktop 3D Scanner and processed with Scan Studio Software (Next Engine Inc., Santa Monica CA). The prototype of the human airway model extends from the oral cavity to lung airway generation 4. It is the wax replica which is the same one as used in the experimental study by Su and Cheng (2006) who developed it from *in vivo* measurements (oral

cavity) and cadavers (trachea-bronchial section).

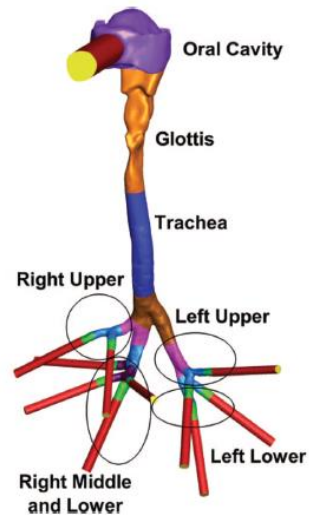


Fig 5.1(a): Model II Geometry (Feng and Kleinstreuer, 2013)

A high quality mesh was generated using commercial meshing software ANSYS ICEM 14.0. The final mesh contained 9.3 million cells with prism layers in the near wall region and tetrahedral elements in the core. Since it is a complex geometry, a large number of cells were required to resolve all the geometrical features as indicated by mesh independence tests.

5.1.2 Governing Equations, Boundary Conditions and Numerical Schemes

OpenFOAM's *simpleFoam* solver was used to solve the Continuity Equation (1), Navier Stokes Equation (2) and three additional transport equations to calculate the eddy viscosity (28-29, see Appendix A) for an incompressible, 3D, transitional flow under steady-state conditions.

A uniform velocity profile was specified at the mouth inlet for each case corresponding to 15L/min, 30L/min and 60L/min. Uniform fixed pressure boundary conditions were specified at the outlets. The no-slip boundary condition was invoked at all airway surfaces. Boundary conditions for all parameters associated with the *kkLOmega* turbulence model were specified as outlined in Section 4.1.2. Higher order schemes (Self Filtered Central Differencing Scheme) and Gauss linear corrected schemes were used to model convective and diffusive terms, respectively.

Particles were distributed uniformly (in terms of surface density) at the mouth inlet with an initial velocity being the same as the air velocity at the inlet. Each particle was assumed to stick to the wall when it is one radius away from the wall. One-way coupling was assumed between the air and particle flow fields.

Traditionally, turbulence is assumed to consist of a collection of randomly directed eddies; hence, an eddy-interaction model (EIM), or dispersion model, was used to simulate the particle trajectories and fluctuating velocities, v' , following Gosman & Ioannides (1981), Matida et al. (2000) or Schuen et al. (1983). Specifically,

$$v' = \xi \left(\frac{2}{3} k \right)^{0.5} \dots\dots\dots (34)$$

where ξ represents random numbers with zero mean, variance of one of Gaussian distribution and k is the turbulence kinetic energy. In this model, each particle is allowed to interact successively with various eddies and the random numbers are maintained constant during one eddy interaction, while the corresponding turbulence intensities vary with the particle position

(MacInnes & Bracco, 1992; Matida et al.,2000). It was also reported that due to the assumption of turbulence isotropy in the current Eddy Interaction Model or Dispersion Model, the fluctuating velocities normal to the wall calculated with Eq. (34) may be higher than the actual values(Kim, Moin & Moser, 1987), which overpredicts the particle deposition(Matida, Finlay, Lange & Gargic, 2002, 2004). Matida et al.(2002, 2004) proposed a near wall correction that can be used to simulate the near-wall particle trajectories i.e., the component of fluctuating velocity normal to the wall (v'_n) can be expressed as:

$$v'_n = f_v \xi \left(\frac{2}{3}k\right)^{0.5} \dots\dots\dots (35)$$

$$f_v = 1 - e^{-0.02y^+} \dots\dots\dots (36)$$

Where y^+ is non-dimensional wall distance, f_v is a damping function component normal to the wall considering the anisotropy of turbulence near the wall (Wang & James, 1999). Usually equation 36 is used for $y^+ < 10$, while $f_v = 1$ elsewhere. Eq. 36 was derived for simple rectangular duct and is expected to work well for other simple geometries.

OpenFOAM's current dispersion model, *StochasticDispersionRAS*, was modified to include near wall corrections as per Eq. 36. Initial set of simulations revealed that Eq. 35, 36 gives good particle deposition results in case of simple geometries but for complicated geometries (Fig 5.1(a)) it severely underpredicted deposition. Based on the comparison between initial set of simulation data on patient specific geometry and experimental data, additional correction factor was derived (Eq. 37) and implemented that gave good results.

$$f_v = 433.92 * Stk * (\exp(0.8754 * r)) * (1 - \exp(-0.02 * y^+)) \dots\dots\dots (37)$$

$$\text{Where, } r = \frac{60 \text{ L/min}}{\text{Simulated Flow Rate in L/min}}$$

5.1.3 Results and Discussions

The solid curve in Fig 5.1(b) is the best fit obtained by nonlinear least square regression method in the SigmaPlot software package (Cheng et al., 1999). The results obtained are for the inlet flow rate of 15L/min. The definition of Stokes Number used in this study is given as (see Cheng et al.,1999):

$$Stk = \frac{d_{ar}^2 U}{9\mu d_h} \dots\dots (38)$$

Here Stk denotes Stokes Number, U is the mean velocity based on the inlet flow rate and mean cross-sectional area (4.43 cm^2), d_h is the minimum hydraulic diameter, i.e., the throat diameter (0.817 cm), and d_{ar} is the particle aerodynamic diameter.

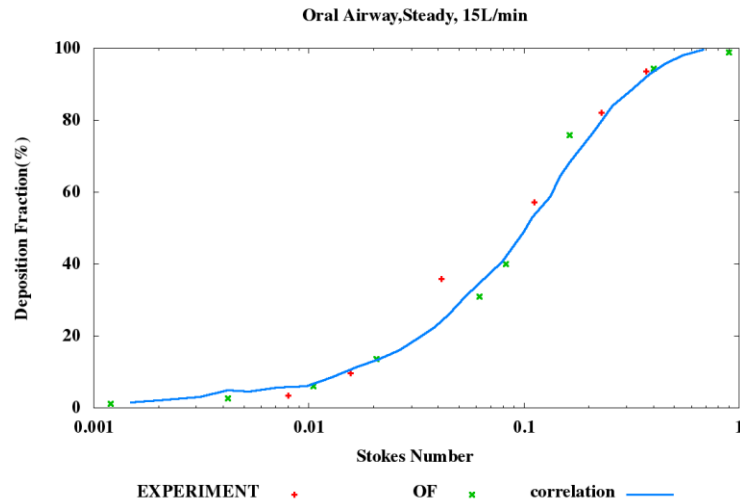


Fig 5.1(b): Model II Oral Airway Deposition Fraction for 15L/min

Particle size range was varied from $2.5 \mu\text{m}$ - $32 \mu\text{m}$ (density = 1000 kg/m^3) to obtain results in the Stokes number range of 0.001 to 1 as per the available experimental data.

Figure 5.1(b) presents the particle deposition for $Q_{\text{in}} = 15\text{L/min}$. Also, the assumption of one-way coupling and subtle differences between the geometries employed in the experimental work and in this computational study further contribute to discrepancies between computational and experimental results.

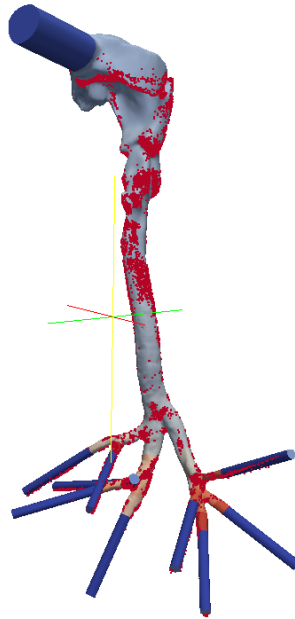


Fig 5.1(c): Model II Particle Deposition Pattern

From Fig 5.1(c) it can be seen most of the particle deposition (red portion in Fig 5.1(c)) takes place in the circular bend (larynx, pharynx region). This is again because the major

mechanism for particle deposition remains inertial impaction. After entering the mouth inlet, particles strike at the near-circular bend in bulk and hence are deposited. Further downstream near the throat region, stronger turbulence dispersion comes into play and the induced velocity perturbations become responsible for particle depositions in and around the throat and trachea regions.

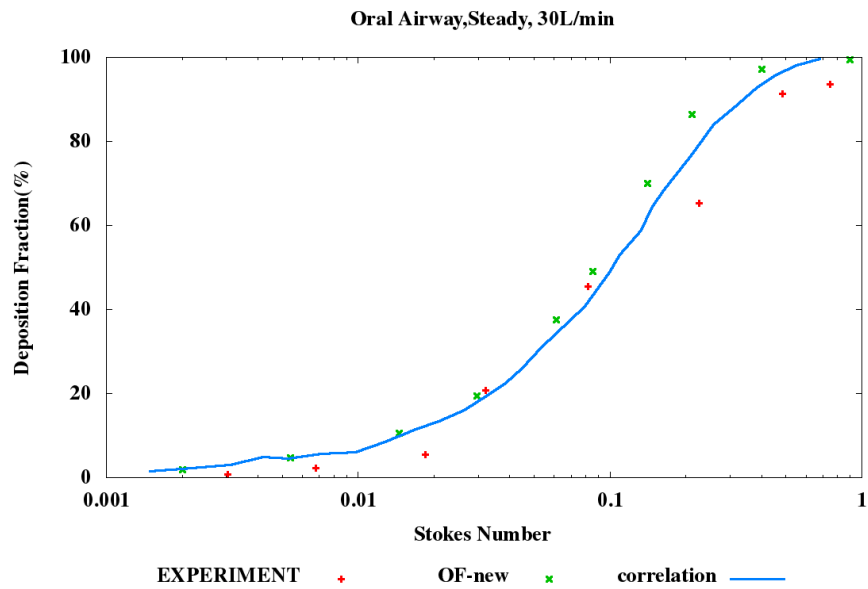


Fig 5.1(d): Model II Oral Airway Deposition Fraction for 30L/min

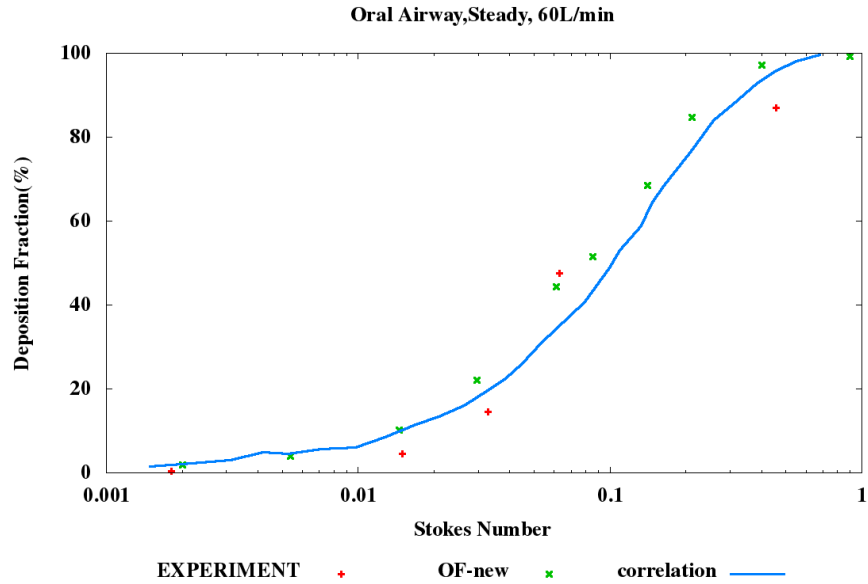


Fig 5.1(e): Model II Oral Airway Deposition Fraction for 60L/min

In summary, fairly good agreement can be seen in particle deposition pattern predicted by OpenFOAM computer simulation model, with improved Dispersion Model, in the patient-specific geometry. Our validated CF-PD simulations of particle transport in the human airways models can provide particle deposition as a function of particle size, inhalation flow rate, and local system geometry. These results are invaluable for physical insight and the analyses of toxic/therapeutic aerosol deposition impacts in the lung.

5.2 Conclusions and Future Works

5.2.1 Conclusions

- Validation Case A (Section 3.1) and Case B (Section 3.2) results suggest that the OpenFOAM computer simulation model can accurately predict flow fields in the laminar range in bifurcating geometries. Hence, OpenFOAM steady-state solver

simpleFoam and transient solver *pimpleFoam* are suitable for solving 3D incompressible Navier Stokes equations for bifurcating tubular structures commonly encountered in biomedical applications.

- Through validation Case C (Section 3.3) and Case D (Section 3.4), an understanding was developed in creating accurate OpenFOAM computer simulation models to simulate particle trajectories using OpenFOAM's Lagrangian Particle Tracking solver *icoUncoupledKinematicParcelFoam*, which numerically solves Newton's Second Law (Equation (3) in Section 2.2), by taking into account pre-calculated flow fields and assumed particle forces. Furthermore, through Case D it was shown that more complicated bifurcating networks (double and triple bifurcations) can be handled with such computer models.
- A new turbulence model, *kkLOmega*, was validated for calculating turbulent flow fields in case of high inhalation flow rates. It was shown in Section 4.1.3 by comparing it with experimental data and ANSYS CFX results that it is *on par* with previously validated LRN $k-\omega$ and SST Transition models (Zhang and Kleinstreuer,2011) for predicting transitional flow.
- In Section 4.2 a one-dimensional Whole-Lung Trumpet Model was presented. Comparison between Whole-Lung Trumpet Model and actual Whole-Lung model reveals that simulations with the Whole-Lung Trumpet Model is 200 times faster in calculating the airflow field. Thus, developing correlations for calculating particle depositions using the Trumpet Model can save a lot of time and computational resources.

5.2.2 Future Works

Based on the work done so far, the following projects are suggested:

- ANSYS ICEM 14.0 which is a commercial grid generation software (ANSYS Inc., Canonsburg, PA) has been used to generate computational meshes in this study, as it has been extensively tested by members of the Computational Multi-Physics Laboratory, to produce quality meshes for CFD solvers. OpenFOAM offers the open-source meshing tool called *snappyHexMesh*, using grid generation models which can be developed and tested for future.
- Particle deposition, in this study, has been calculated in steady flow fields, assuming one-way coupling. In the future, transient airflow fields should be considered, which will also allow to incorporate particle-fluid interaction and/or particle-particle interaction models.
- The Trumpet Model $\overline{F_{rad}}$ correlation can be extended to cover entire range of particle sizes i.e microspheres ($d_p > 1 \mu\text{m}$) as well as nano-particles ($d_p < 100\text{nm}$).
- In this study only microspheres were considered. Nano-particles can be simulated by solving the convection-diffusion equation which can be done with OpenFOAM's *scalarTransportFoam* solver, but it may need modification in case turbulence has to be included (Krause et al., 2012).
- All the airway models considered in this study were assumed to have rigid walls. In reality, walls are constantly expanding and contracting. This kind of problems falls under the domain of Fluid-Surface Interaction (FSI). Currently, there is no solver in

- OpenFOAM that can simulate this kind of coupled fluid-structural phenomenon. Thus, efforts should be made to develop and implement new FSI solvers in OpenFOAM to simulate such phenomena. This will also be a novel contribution to the open-source CFD community.
- There is a scope of improvement in the performance of OpenFOAM software (see Section 3.6). Better numerical/discretization/interpolation schemes can be programmed and integrated with OpenFOAM source code to bring its computation speed at par with commercial CFD packages.

References

- Bushi,D.,Grad,Y.,Einav,S.,Yodfat,O.,Nishri,B., & Tanne,D (2005).Hemodynamics Evaluation of Embolic Trajectory in an Arterial Bifurcation:An In-vitro Experimental Model,36,2696-2700
- Chan, T.L. & Lippmann,M. (1980). Experimental measurements and empirical modeling of the regional deposition of inhaled particles in humans. *Journal of Applied Physiology*, 94(5), 1719-1725.
- Cheng,Y.S., Zhou.Y., & Chen,T.B.(1999). Particle Deposition in a Cast of Human Oral Airways, 31,286-300.
- Choi, J.I & Kim, C.S., (2007). Mathematical Analysis of Particle Deposition in Human Lungs: An Improved Single Path Transport Model, 19, 925-939.
- Emmett, P. C., Aitken, R. J., & Hannan, W. J (1982). Measurement of total and regional deposition of inhaled particles in the human respiratory tract. *Journal of Aerosol Science*, 13, 549-560.
- Foord, N.,Black, A & Walsh, M.(1978). Regional deposition of 2.5-7 μ m diameter inhaled particles in healthy non-smokers. *Journal of Aerosol Science*, 9, 343-357.
- Kim, C.S & Fisher, D.M (1999). Deposition of aerosol particles in successively bifurcating models. *Aerosol Science and Technology*, 31, 198-220.

- Lippmann, M.(1977). Regional deposition of particles in human respiratory tract. Handbook of physiology-reaction to environmental agents (pp. 213-232). Bethesda,MD:American Physiology Society.
- Matida, E.A., Finlay, W.H., Lange, C.F., & Grgic, B.(2002). Improving numerical simulations of particle deposition in the mouth-throat using near-wall corrections to turbulence modeling. 21th AAAR Conference, 5-8 October 2002, Charlotte, North Carolina.
- Oldham, M.J.,Phalen,R.F., & Heistracher,T.(2000). Computational Fluid Dynamics prediction and experimental results for particle deposition in an airway model. Aerosol Science and Technology, 32, 61-71.
- Walters,K.D & Cokljat,D(2008).A Three-Equation Eddy-Viscosity Model for Reynolds-Averaged Navier- Simulations of Transitional Flow, Journal of Fluid Engineering,130,1-14
- Weibel, E. R.(1963). Morphometry of the human lung. New York: Academic Press.
- Zhang,Z & Kleinstreuer,C.(2003). Low-Reynolds-Number Turbulent Flows in Locally Constricted Conduits: A Comparison Study, 41,831-840.
- Zhang Z., Kleinstreuer C., & Kim C.S., Comparison of micro and nano-size particle depositions in a human upper airway model, 36, 211-233

- Zhang, Z., Kleinstreuer, C., & Kim, C.S. (2001). Cyclic micron-size particle inhalation and deposition in a triple bifurcation lung airway model
- Zhang, Z., Kleinstreuer, C., & Kim, C.S. (2009). Comparison of analytical and CFD models with regard to micron particle deposition in a human 16-generation tracheobronchial airway model. *Aerosol Science and Technology*, 40, 16-28
- Zhao, Y. & B.B. Lieber. (1998). Oscillatory Flow in a Symmetric Bifurcation Airway Model. *Annals of Biomedical Engineering*, 26, 821-830
- Zhao, Y. & B.B. Lieber. (1994). Steady inspiratory flow in a model symmetric bifurcation. *J. Biomech. Eng.*, 116, 488-496.

APPENDICES

APPENDIX A

A.1 *kkLOmega* Turbulence Model Equations

In this section the governing equations associated with *kkLOmega* turbulence model equations are summarized. Three additional model transport equations are solved for the turbulent kinetic energy (k_T), and the scale-determining variable (ω), defined here as $\omega = \varepsilon / k_T$, where ε is the isotropic dissipation. The transport equations are

$$\frac{Dk_T}{Dt} = P_{k_T} + R_{BP} + R_{NAT} - \omega k_T - D_T + \frac{\partial}{\partial x_j} \left[\left(\nu + \frac{\alpha_T}{\sigma_k} \right) \frac{\partial k_T}{\partial x_j} \right] \dots (39)$$

$$\frac{Dk_L}{Dt} = P_{k_L} - R_{BP} - R_{NAT} - D_L + \frac{\partial}{\partial x_j} \left[\nu \frac{\partial k_L}{\partial x_j} \right] \dots (40)$$

$$\frac{D\omega}{Dt} = C_{\omega 1} \frac{\omega}{k_T} P_{k_T} + \left(\frac{C_{\omega R}}{f_W} - 1 \right) \frac{\omega}{k_T} (R_{BP} + R_{NAT}) - C_{\omega 2} \omega^2 + C_{\omega 3} f_{\omega} \alpha_T f_{\omega} \frac{\sqrt{k_T}}{d^3} + \frac{\partial}{\partial x_j} \left[\left(\nu + \frac{\alpha_T}{\sigma_{\omega}} \right) \frac{\partial \omega}{\partial x_j} \right] \dots (41)$$

The various terms in the model equations represent production, destruction, and transport mechanisms. Note that the new model uses inverse turbulent time-scale (ω) rather than the dissipation rate (ε), in contrast to the original version of Walters and Leylek (2004). It has been noted previously that this form yields improved accuracy in the transition region Walters and Leylek (2005). In the ω equation, the fully turbulent production, destruction, and gradient transport terms (first, third, and fifth terms on the right-hand side of Eq. 39) are analogous to the similar terms in the k_T and k_L equations and are similar to terms that appear in other $k-\omega$ model forms. The transition production term (second term on right-hand side) is intended to produce a reduction in turbulence length scale during the transition breakdown process. A

similar term was included in the ε equation of the original model (Walters and Leylek, 2004).

The fourth term on the

right - hand side was included in order to decrease the length scale in the outer region of the turbulent boundary layer, which is necessary to ensure correct prediction of the boundary layer wake region(Walter and Leylek, 2004).

The total fluctuation kinetic energy is $k_{TOT} = k_T + k_L$. The production of turbulent and laminar kinetic energy by mean strain is modeled as:

$$P_{k_T} = \nu_{T,s} S^2 \dots\dots\dots (42)$$

$$P_{k_L} = \nu_{T,l} S^2 \dots\dots\dots (43)$$

The “small-scale” eddy-viscosity concept follows Walter and Leylek (2004), and is defined as:

$$\nu_{T,s} = f_\mu f_{INT} C_\mu \sqrt{k_{T,s} \lambda_{eff}} \dots\dots\dots (44)$$

Where $k_{T,s}$ is the effective small-scale turbulence.

$$k_{T,s} = f_{SS} f_W k_T \dots\dots\dots (45)$$

The kinematic wall effect is included through an effective (wall-limited) turbulence length scale λ_{eff} and damping function f_W .

$$\lambda_{eff} = \min(C_\lambda d, \lambda_T) \dots\dots\dots (46)$$

$$\lambda_T = \frac{\sqrt{k_T}}{\omega} \dots\dots\dots (47)$$

$$f_W = \frac{(\lambda_{eff})}{(\lambda_T)} \dots\dots\dots (48)$$

The viscous wall effect is incorporated through the viscous damping function, which is computed in terms of the effective turbulence Reynolds number.

$$f_v = 1 - \exp\left(-\frac{\sqrt{\text{Re}_T}}{A_v}\right) \dots\dots\dots(49)$$

$$\text{Re}_T = \frac{f_w^2 k_T}{\nu \omega} \dots\dots\dots(50)$$

The shear-sheltering effect discussed in the previous subsection is included in the damping function f_{ss} .

$$f_{ss} = \exp\left[-\left(\frac{C_{ss} \nu \Omega}{k_T}\right)^2\right] \dots\dots\dots(51)$$

The turbulent viscosity coefficient C_μ is defined to satisfy the realizability constraint following Shih et al. (1995):

$$C_\mu = \frac{1}{A_0 + A_s \left(\frac{S}{\omega}\right)} \dots\dots\dots (52)$$

The effect of intermittency on the turbulence production is included through an empirical intermittency damping function.

$$f_{INT} = \min\left(\frac{k_L}{C_{INT} k_{TOT}}, 1\right) \dots\dots\dots (53)$$

The production of laminar kinetic energy (k_L) is assumed to be governed by the large-scale near-wall turbulent fluctuations, based on the correlation of pretransitional fluctuation growth with freestream low-frequency wall-normal turbulent fluctuations. The large-scale turbulence contribution is:

$$k_{T,l} = k_T - k_{T,s} \dots\dots\dots (54)$$

Where the small-scale contribution is defined by Eq.(43). The production term is

$$P_{k_L} = \nu_{T,l} S^2 \dots\dots\dots(55)$$

Where

$$\nu_{T,l} = \min \left\{ f_{\tau,l} C_{11} \left(\frac{\Omega \lambda_{eff}^2}{2} \right) \sqrt{k_{T,l} \lambda_{eff}} + \beta_{TS} C_{12} \text{Re}_\Omega d^2 \Omega, \frac{0.5(k_L + k_{T,l})}{S} \right\} \dots\dots\dots(56)$$

The limit is applied to ensure satisfaction of the realizability constraint for the total Reynolds stress contribution. The production term is comprised of two parts—the first addresses the development

of Klebanoff modes and the second addresses self-excited(i.e., natural) modes.

$$\text{Re}_\Omega = \frac{d^2 \Omega}{\nu} \dots\dots\dots(57)$$

$$\beta_{TS} = 1 - \exp\left(-\frac{\max(\text{Re}_\Omega - C_{TS,crit}, 0)^2}{A_{TS}}\right) \dots\dots(58)$$

$$f_{\tau,l} = 1 - \exp\left[-C_{\tau,l} \frac{k_{T,l}}{\lambda_{eff}^2 \Omega^2}\right] \dots\dots\dots(59)$$

The anisotropic _near-wall_ dissipation terms for k_T and k_L take a common form.

$$D_T = \nu \frac{\partial \sqrt{k_T}}{\partial x_j} \frac{\partial \sqrt{k_T}}{\partial x_j} \dots\dots\dots(60)$$

$$D_L = \nu \frac{\partial \sqrt{k_L}}{\partial x_j} \frac{\partial \sqrt{k_L}}{\partial x_j} \dots\dots\dots(61)$$

The turbulent transport terms in the k_T and ω equations include an effective diffusivity α_T

defined as:

$$\alpha_T = f_v C_{\mu, std} \sqrt{k_{T,s}} \lambda_{eff} \dots\dots\dots (62)$$

The boundary layer production term (intended to reproduce proper behavior of the boundary layer wake region) includes a kinematic damping function of the form

$$f_\omega = 1 - \exp[-0.41 * (\frac{\lambda_{eff}}{\lambda_T})^4] \dots\dots\dots (63)$$

The remaining terms in the transport equations are related to the laminar-to-turbulent transition mechanism in the model. As mentioned above, transition occurs as a transfer of energy from k_L to k_T , with a concurrent reduction in turbulence length scale from the freestream value to the value found in an equilibrium turbulent boundary layer. The model terms R_{BP} and R_{NAT} appear with opposite signs in the kT and kL equations and represent bypass and natural transition, respectively. The model forms are

$$R_{BP} = C_R \beta_{BP} k_L \omega / f_W \dots\dots\dots (64)$$

$$R_{NAT} = C_{R,NAT} \beta_{NAT} k_L \Omega \dots\dots\dots (65)$$

Transition initiation is governed by the threshold functions β_{BP} and β_{NAT} . As discussed in the previous section, transition in both cases is assumed to initiate when the characteristic time-scale for turbulence production is smaller than the viscous diffusion timescale of the pretransitional fluctuations. The forms used are

$$\beta_{BP} = 1 - \exp(-\frac{\phi_{BP}}{A_{BP}}) \dots\dots\dots (66)$$

$$\phi_{BP} = \max[(\frac{k_T}{v\Omega} - C_{BP,crit}), 0] \dots\dots\dots (67)$$

$$\beta_{NAT} = 1 - \exp\left(-\frac{\phi_{NAT}}{A_{NAT}}\right) \dots\dots\dots (68)$$

$$\phi_{NAT} = \max[(\text{Re}_\Omega - C_{NAT,crit}), 0] \dots\dots\dots (69)$$

$$f_{NAT,crit} = 1 - \exp\left(-C_{NC} \frac{\sqrt{k_L} d}{\nu}\right) \dots\dots\dots (70)$$

Note that the function $f_{NAT,crit}$ is included so that the amplitude of the pretransitional fluctuations influences the initiation of natural transition in an appropriate manner. The turbulent viscosity used in the momentum equations is the sum of the small-scale and large-scale contributions defined above.

$$\nu_T = \nu_{T,s} + \nu_{T,l} \dots\dots\dots (71)$$

Table A.1: *kkLOmega* Turbulence Model Constants

Constant	Value
A_0	4.04
A_s	2.12
A_ν	6.75
A_{BP}	0.6
A_{NAT}	200
A_{TS}	200

Table A.1: Continued

$C_{NAT,crit}$	1250
C_{INT}	0.75
$C_{TS,crit}$	1000
$C_{R,NAT}$	0.02
C_{11}	$3.4 \cdot 10^{-6}$
C_{12}	$1.0 \cdot 10^{-6}$
C_R	0.12
$C_{\alpha,\theta}$	0.035
C_{SS}	1.5
$C_{\tau,1}$	4360
$C_{\omega 1}$	0.44
$C_{\omega 2}$	0.92
$C_{\omega R}$	1.5
$C_{\omega 3}$	0.3
C_{λ}	2.495
$C_{\mu,std}$	0.09

Table A.1: Continued

σ_ω	1.17
-----------------	------